Author/s:
Liang, C;Zhang, S;Robinson, D;Ploeg, MV;Wilson, R;Nah, J;Taylor, D;Beh, S;Lim, R;Sun, L;Muoio, DM;Stroud, DA;Ho, L

Title:
Mitochondrial microproteins link metabolic cues to respiratory chain biogenesis

Date:
2022-08-16

Citation:
Liang, C., Zhang, S., Robinson, D., Ploeg, M. V., Wilson, R., Nah, J., Taylor, D., Beh, S., Lim, R., Sun, L., Muoio, D. M., Stroud, D. A. & Ho, L. (2022). Mitochondrial microproteins link metabolic cues to respiratory chain biogenesis. Cell Reports, 40 (7), https://doi.org/10.1016/j.celrep.2022.111204.

Persistent Link:
https://hdl.handle.net/11343/322103

Cell Reports

Article

Mitochondrial microproteins link metabolic cues to respiratory chain biogenesis

Graphical abstract

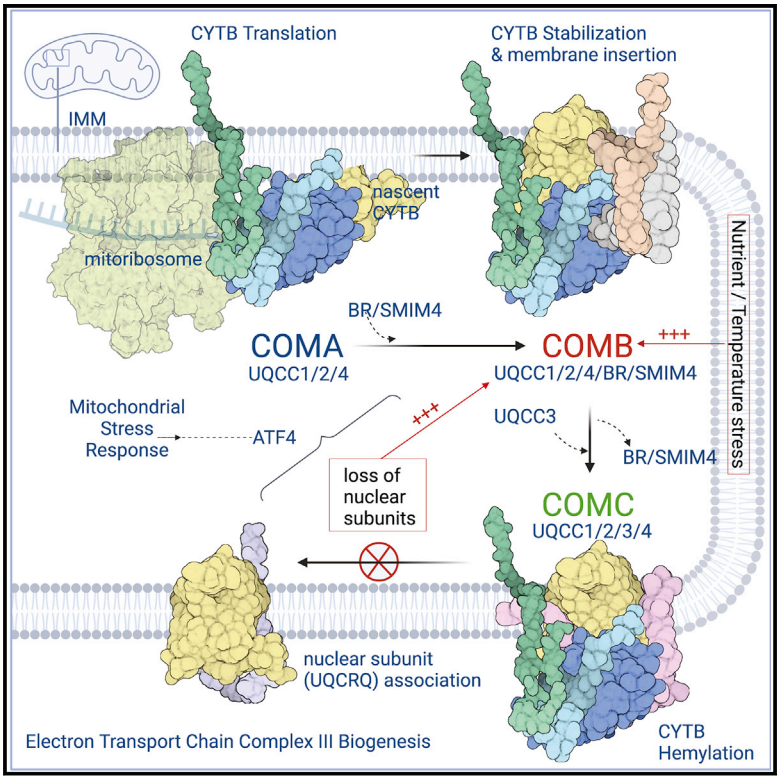

Highlights

- COMA, COMB, and COMC complexes are required for ETC CIII assembly
- COMB comprises of microproteins BRAWNIN and SMIM4 and promotes nascent CIII stability
- COMB tunes CIII levels according to nutrient and nuclear CIII subunit availability
- Early CIII assembly is a node for cells to sense and respond to mitochondrial stress

Authors

Chao Liang, Shan Zhang, David Robinson, ..., Deborah M. Muoio, David A. Stroud, Lena Ho

Correspondence

lena@ho-lab.org

In brief

Mitochondria are enriched in microproteins of unknown functions. Here, Liang et al. show that some of these microproteins nucleate complexes that are crucial for the construction of the electron transport chain and for ensuring that the energy supply is regulated by energy demand.

Liang et al., 2022, Cell Reports *40*, 111204
August 16, 2022
https://doi.org/10.1016/j.celrep.2022.111204

CellPress

Cell Reports

CellPress
OPEN ACCESS

Article

Mitochondrial microproteins link metabolic cues to respiratory chain biogenesis

Chao Liang,[1,8] Shan Zhang,[1,2,8] David Robinson,[3] Matthew Vander Ploeg,[4] Rebecca Wilson,[4] Jiemin Nah,[1] Dale Taylor,[3,7] Sheryl Beh,[1] Radiance Lim,[1] Lei Sun,[1] Deborah M. Muoio,[4] David A. Stroud,[3,5] and Lena Ho[1,6,9,*]

[1]Cardiovascular and Metabolic Diseases, Duke-NUS Medical School, 169857 Singapore, Singapore
[2]Department of Biochemistry, Department of Cardiology of First Affiliated Hospital, Zhejiang University School of Medicine, Hangzhou, China
[3]Department of Biochemistry and Pharmacology, the Bio21 Molecular Science and Biotechnology Institute, University of Melbourne, 30 Flemington Road, Parkville, VIC 3052, Australia
[4]Departments of Medicine and Pharmacology and Cancer Biology, Sarah W. Stedman Nutrition and Metabolism Center and Duke Molecular Physiology Institute, Duke University, Durham, NC 27701, USA
[5]Murdoch Children's Research Institute, the Royal Children's Hospital, 50 Flemington Road, Parkville, VIC 3052, Australia
[6]Institute of Molecular and Cell Biology, A*STAR, 61 Biopolis Dr, 138673 Singapore, Singapore
[7]Present address: Institute for Health and Sport (IHES), Victoria University, Melbourne, VIC 2011, Australia
[8]These authors contributed equally
[9]Lead contact
*Correspondence: lena@ho-lab.org
https://doi.org/10.1016/j.celrep.2022.111204

SUMMARY

Electron transport chain (ETC) biogenesis is tightly coupled to energy levels and availability of ETC subunits. Complex III (CIII), controlling ubiquinol:ubiquinone ratio in ETC, is an attractive node for modulating ETC levels during metabolic stress. Here, we report the discovery of mammalian Co-ordinator of mitochondrial CYTB (COM) complexes that regulate the stepwise CIII biogenesis in response to nutrient and nuclear-encoded ETC subunit availability. The COMA complex, consisting of UQCC1/2 and membrane anchor C16ORF91, facilitates translation of CIII enzymatic core subunit CYTB. Subsequently, microproteins SMIM4 and BRAWNIN together with COMA subunits form the COMB complex to stabilize nascent CYTB. Finally, UQCC3-containing COMC facilitates CYTB hemylation and association with downstream CIII subunits. Furthermore, when nuclear CIII subunits are limiting, COMB is required to chaperone nascent CYTB to prevent OXPHOS collapse. Our studies highlight CYTB synthesis as a key regulatory node of ETC biogenesis and uncover the roles of microproteins in maintaining mitochondrial homeostasis.

INTRODUCTION

The mammalian electron transport chain (ETC) is formed by complexes I–IV located in the inner mitochondrial membrane (IMM) and is responsible for the production of cellular ATP by oxidative phosphorylation (OXPHOS). Complex III (CIII) occupies a central position in the respiratory chain by receiving electrons from $CoQH_2$ for the reduction of cytochrome C (Vercellino and Sazanov, 2021). Notably, CoQ not only receives electrons from complexes I (CI) and II (CII), but also connects fatty acid oxidation, pyrimidine synthesis, and the glycerol phosphate shuttle with OXPHOS. As such, CIII is responsible for the regeneration of CoQ and maintaining optimal $CoQH_2$:CoQ balance for OXPHOS and optimal cell growth (Martínez-Reyes et al., 2020; Wang and Hekimi, 2016; Weinberg et al., 2019). Furthermore, CIII is required for the assembly of other ETC complexes, including CI and complex IV (CIV) (Acìn-Pérez et al., 2004; Diaz et al., 2012; Protasoni et al., 2020).

ETC biogenesis is tightly coordinated by energy status. Metabolic sensors such as AMP-activated kinase (AMPK) and SIRTUIN1 respond to increased AMP/ATP and NAD^+/NADH ratios, respectively, signaling energy depletion, and activate downstream signaling cascades to increase energy production (Cantó and Auwerx, 2009). Chief among these is the master regulator of energy homeostasis—peroxisome proliferator activated receptor-γ coactivator 1-α (PGC-1α) (Handschin and Spiegelman, 2006; Puigserver et al., 1998), which is activated in response to cold stress, exercise, or starvation. PGC-1α coactivates a wide variety of transcription factors to upregulate genes required for mitochondrial biogenesis and increased substrate use (Handschin and Spiegelman, 2006; Scarpulla, 2002). It is therefore well known that, in response to metabolic perturbations, cells activate broad programs of transcriptional changes to increase mitochondrial mass and output to restore energy homeostasis (Balsa et al., 2019; Mootha et al., 2004; Scarpulla, 2008; Schreiber et al., 2004; Wu et al., 1999). However, whether mechanisms exist to regulate adaptive biogenesis of individual ETC complexes in response to metabolic challenge is unknown. Because of the central function of CIII in ETC, its biogenesis is an attractive node for regulating the overall activity of the ETC.

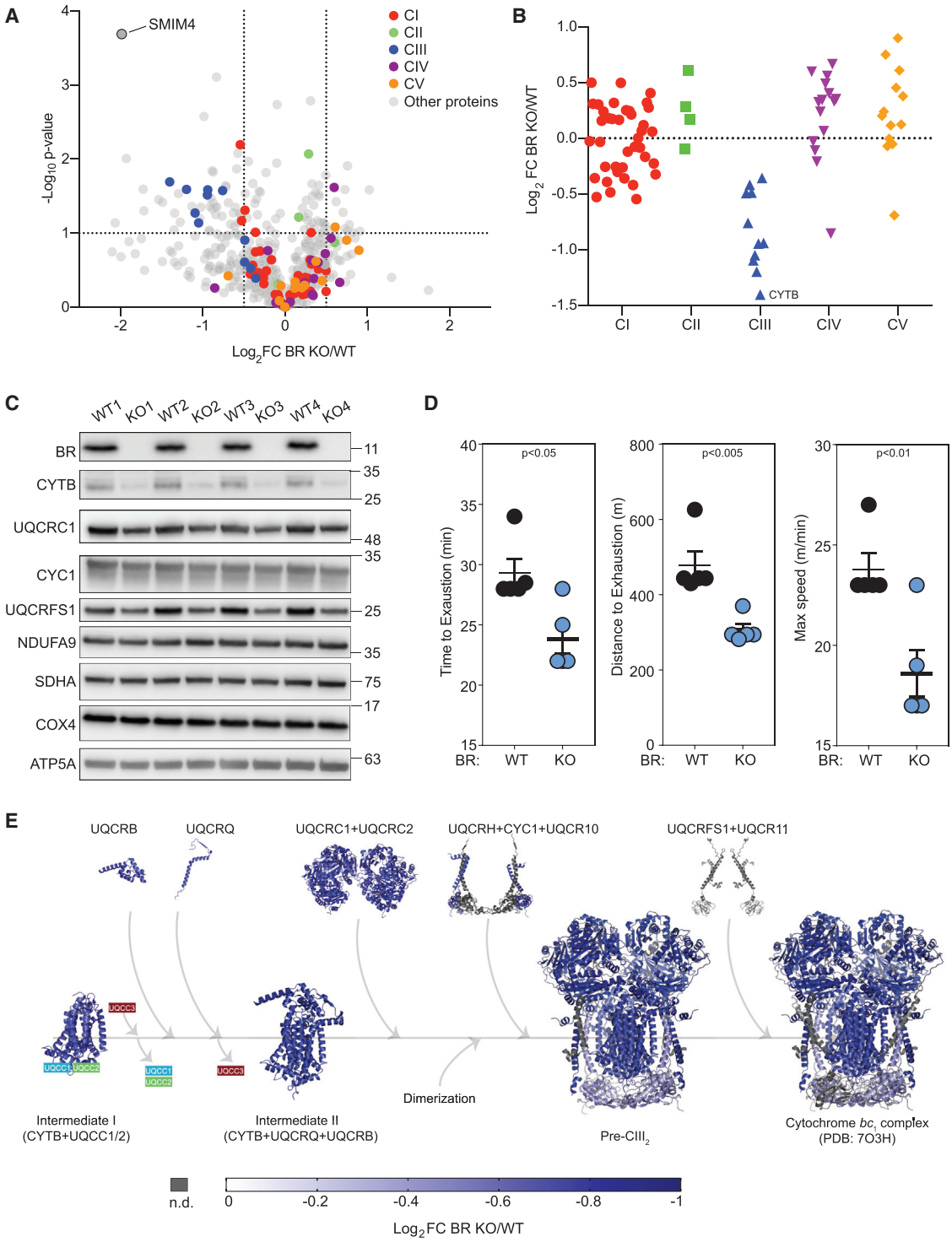

Figure 1. Mammalian BR is required for CIII biogenesis

(A) Volcano plot showing the relative abundance of heart mitochondrial proteins in BR KO mouse as determined by mass spectrometry (MS). Paired littermates of four WT and four BR KO female mice were sacrificed at 9 weeks. Subunits from individual ETC complexes were highlighted with indicated colors. Mouse Mitocarta 2.0 proteins are presented. Data presented as mean, n = 4 biological replicates. p values are from two-tailed unpaired *t* tests.

(B) Protein abundances of RC complex subunits grouped by complexes in data shown in (A).

(C) Immunoblotting analysis of representative RC complex subunits in BR KO mouse heart mitochondrial lysates.

(legend continued on next page)

In addition to being energy responsive, ETC biogenesis requires the stoichiometrical match of nuclear and mitochondrial subunits. This is achieved by controlling mtDNA-encoded ETC subunits translation via translational activators and feedback control mechanisms like TACO1/COX14 for CIV and Cbs1/Cbp3-Cbp6 for CIII in yeast (Hildenbeutel et al., 2014; Salvatori et al., 2020; Weraarpachai et al., 2009). Mitochondrial translation is further coupled to import of nuclear-encoded subunits, such that a stall in mitochondrial import triggers a corresponding pause in mitochondrial translation to maintain coordinated production (Priesnitz and Becker, 2018). For instance, the MITRAC complex holds nascent COX1 (a core mtDNA-encoded subunit in CIV) in an assembly intermediate with the mito-ribosome, stalling *COX1* mRNA translation until nuclear-encoded COX4 is imported (Richter-Dennerlein et al., 2016). While such mechanisms have been well characterized for early steps of mammalian CIV assembly, it is unclear if other complexes require similar strategies of mito-nuclear coordination and if an equivalent of the MITRAC complex exists for other ETC complexes.

Small open reading frame (ORF)-encoded peptides (SEPs) are small nuclear encoded proteins arising from often unannotated or hitherto uncharacterized small ORFs in mRNAs, noncoding RNAs or UTRs of conventional mRNAs. We previously reported a preponderance of SEPs localized to the mitochondrion. Also known as mito-SEPs, we found that these small proteins are preferentially employed by the ETC—where mito-SEPs constitute approximately 28% of the known proteins required for the ETC, whereas they make up less than 2% of the known proteome (Zhang et al., 2020). We demonstrated that BRAWNIN—a prototypical mito-SEP—is required for CIII assembly. Brawnin (*br*) deficiency in zebrafish leads to complete CIII loss and mitochondrial disease resembling GRACILE syndrome (Zhang et al., 2020). However, the molecular mechanisms underpinning BR's role in CIII assembly is unclear. Assembly of CIII is assisted by assembly factors in multiples stages (Ghezzi et al., 2011; Lobo-Jarne et al., 2018; Lonlay et al., 2001; Vasseur et al., 2021). CYTB, the mtDNA-encoded core enzymatic subunit of CIII, is the first protein to be synthesized during assembly. Assembly factors required for CYTB biogenesis have been extensively studied in yeast (García-Guerrero et al., 2018; Gruschke et al., 2011, 2012; Salvatori et al., 2020). While they have been identified in mammals (Tucker et al., 2013; Wanschers et al., 2014), how these early steps of CYTB synthesis are achieved in mammalian CIII biogenesis is unknown, along with the identities of the proteins and complexes involved. Furthermore, whether this step in mammalian CIII biogenesis acts as a sensor to regulate CIII production in response to metabolic cues, or as a regulatory node for nuclear-mitochondrial coordination, is unknown. Here, we sought to delineate the regulatory events underlying mammalian CIII assembly and the molecular mechanism of BRAWNIN in CIII biogenesis.

RESULTS

BRAWNIN is required for early CIII biogenesis

We previously demonstrated that Brawnin deficiency in zebrafish led to complete CIII loss and mitochondrial disease (Zhang et al., 2020). To understand if this requirement is conserved in mammals, we generated a CRISPR/Cas9-mediated BRAWNIN (BR) knockout (KO) mouse (Figures S1A and S1B). Unlike *br* KO zebrafish, BR KO mice showed no difference in growth trajectory compared with wild-type or heterozygotes (Figure S1C). There was also no significant deviation from the expected number and gender of homozygotes derived from intercrosses (Figure S1D). To verify the requirement for BR in mammalian CIII biogenesis, we isolated cardiac mitochondria and performed label-free quantitative proteomic analysis (Figures 1A, 1B and Table S1) and western blot (Figure 1C), confirming that BR deficiency in mouse caused specific CIII depletion, despite the lack of an overt growth phenotype, while subunits of CI, CII, CIV, and CV were not affected (Figures 1A–1C and S1E). Furthermore, blue native (BN)-PAGE analysis of DDM-solubilized mitochondria confirmed that fully assembled CIII dimers were significantly decreased in BR KO mice (Figure S1F). Digitonin-solubilized mitochondria BN-PAGE showed similar downregulation of CIII subunits across all assembly stages, with minimal changes in other complexes (Figure S1H). The observed CIII deficiency in BR KO mice led to a mild increase in blood lactate levels (Figure S1G) and significantly decreased exercise tolerance (Figure 1D), demonstrating the physiological requirement for mammalian BR.

CIII assembly follows a stepwise assembly from intermediate I to a fully assembled $CIII_2$ dimer (Figure 1E) (Atkinson et al., 2010, 2011; Crivellone et al., 1988; Cui et al., 2012; Gruschke et al., 2012; Stephan and Ott, 2020; Zara et al., 2004). By plotting the fold change of each subunit across the assembly intermediates, we found that the BR KO affected abundance of CIII subunits from as early as the intermediate II consisting of CYTB, UQCRQ, and UQCRB (Figure 1E). Of these, CYTB levels were the lowest in BR KO mice, suggesting that BR deficiency in the mouse results in very early CIII assembly defect, possibly during CYTB synthesis (Figure 1B).

BR, SMIM4, and C16ORF91 form an approximately 240-kDa COMB complex

Since BR is not a subunit of mature CIII (Zhang et al., 2020), we next asked if BR belonged to a complex that mediates early CIII biogenesis. In BN-PAGE of digitonin-solubilized mitochondria extracted from mouse heart and C2C12 myoblasts, BR migrates as an approximately 240-kDa complex in addition to its monomeric form (Figure 2A). To define the biochemical identity of this complex, we performed BR immunoprecipitation (IP)/mass spectrometry (MS) analysis using BR-FLAG overexpressed in heart mitochondria solubilized in digitonin (Figure 2B). The top hits of the interactome were mito-SEPs SMIM4 and

(D) Exercise capacity of male BR KO mice (20 weeks old) measured by forced treadmill running using littermate WT controls. Exhaustion time, distance, and maximum running speed were plotted. Data are represented as mean ± standard error of the mean, n = 5 biological replicates. p values are from two-tailed unpaired *t* tests.

(E) Schematic presentation of mammalian CIII assembly inferred from studies in yeast. Subunits were colored according to their relative abundance in BR KO mouse hearts. Structure model: PDB 7O3H.

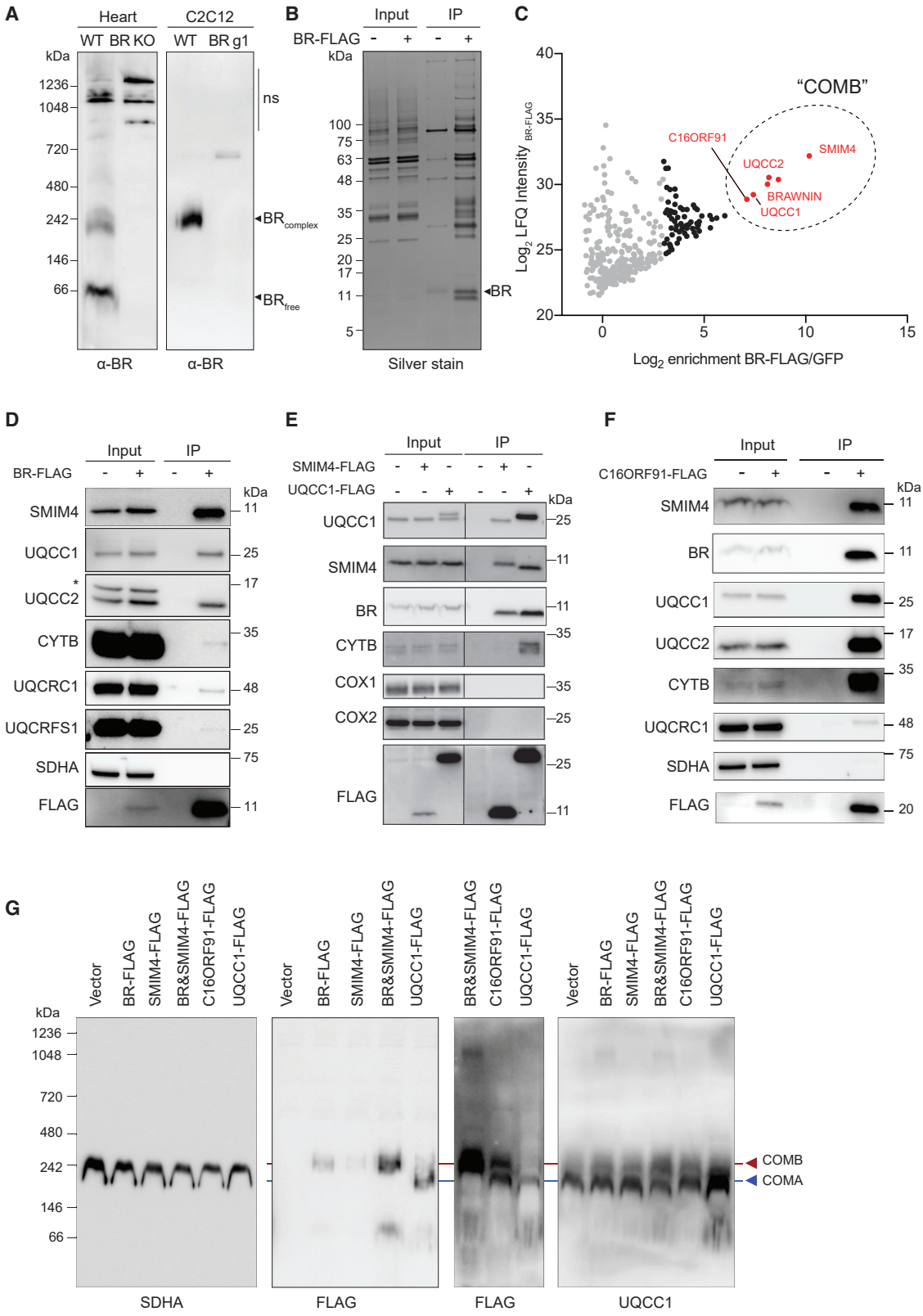

(legend on next page)

C16ORF91, which are uncharacterized SEPs previously identified by us (Zhang et al., 2020), and UQCC1 and UQCC2 (Figure 2C and Table S2). These interactions were verified by IP-western blotting (Figure 2D). Furthermore, reciprocal IP of SMIM4, UQCC1, and C16ORF91 detected BR and each other (Figures 2E and 2F), confirming their membership in the same complex. Other enriched interacting partners were predominantly ETC components (Figure S2A). UQCC1 and UQCC2 are the mammalian homologues of yeast Cbp3 and Cbp6, respectively, and are required for yeast cytb translation. In humans, mutations in UQCC2 lead to mitochondrial disease owing to CIII deficiency (Tucker et al., 2013), suggesting that the BR-containing complex is involved in CYTB translation. Differential detergent extraction (Figures S2B and S2C) demonstrates that SMIM4 and C16ORF91, hitherto uncharacterized, are indeed IMM proteins, consistent with the predicted presence of single-pass transmembrane domains (TMDs). Proteinase K protection assays (Figures S2D and S2E) further suggest that the C-termini of both proteins reside in the intermembrane space, since the antibodies against both proteins recognize their C termini. Consistent with their inclusion in the BR-containing complex, SMIM4, C16ORF91, UQCC1, and UQCC2 co-migrated with BR in the approximately 240-kDa complex in BN-PAGE (Figure 2G). Using an orthogonal approach of sucrose gradient fractionation of purified mitochondria, SMIM4 and UQCC1 co-sedimented with BR (Figure S2F), further supporting them being part of the same complex. Since yeast homologues of UQCC1 and 2 (Cbp3 and 6) are required for CYTB translation—together with our observation of profound CYTB downregulation in BR KO (Figure 1B), we postulated that the COMB complex regulates CYTB synthesis. Therefore, we named the 240-kDa complex "co-ordinator of mitochondrial CYTB biogenesis" or "COMB."

Notably, UQCC1 and UQCC2 do not co-migrate exclusively with COMB. In BN-PAGE, UQCC1 and UQCC2 reside in two distinct complexes, one at COMB and one that migrates at approximately 200 kDa (Figure 2G). Specificity of the UQCC1 bands in BN-PAGE were validated using a UQCC1 KO cell line (Figure S2G). Because this smaller complex seems to lack SMIM4 and BR and is more akin to the yeast Cbp3/6 complex that mediates translational activation, we designated it as "COMA."

Mito-SEPs are required for COM complex stability and membrane association

To confirm the biochemical composition of COMA, we performed anti-FLAG IP/MS in wild-type (WT) and BR KO C2C12 mitochondria expressing UQCC1-FLAG (Figure 3A). In WT mitochondria, UQCC1-FLAG recovered SMIM4, BR, UQCC2, and C16ORF91, while in KO mitochondria, UQCC1-FLAG recovered only UQCC2 and C16ORF91 (Figure 3A). Therefore, the COMA complex can be defined as COMB without BR/SMIM4 (Figure S3A).

To understand the contribution of the mito-SEPs BR, SMIM4 and C16ORF91 to COMB and COMA, we performed BN-PAGE of BR KO, SMIM4 KO, and C16ORF91 KO C2C12 cells and examined the stability and migration of UQCC. Strikingly, deletion of C16ORF91 (Figure S3B) attenuated both COMA and COMB and collapsed UQCC1 to free monomers without affecting total levels (Figures 3B and S3C), indicating that C16ORF91 is required for the integrity of both COMA and COMB. Consequently, C16ORF91 KO cells have a marked decrease in mature CIII dimers (Figure 3B). UQCC1 and 2 are bound to the IMM despite the lack of TMDs (Figure 3C). We hypothesized that C16ORF91, which is a predicted single-pass TMD-containing protein, anchors UQCC1/2 to the IMM and serves as a scaffold for COMA/B complexes. Indeed, in C16ORF91 KO cells, UQCC1 is found predominantly in the soluble fractions of sodium carbonate and potassium chloride-extracted mitochondrial membranes (Figure 3C), consistent with the dissociation of UQCC1 into free un-complexed form (Figure 3B). Hence, C16ORF91 (renamed as UQCC4) anchors UQCC1-containing COMA and COMB complexes to the IMM where they are required for CYTB synthesis.

In contrast, BR and SMIM4 deletion led to the depletion of COMB but not COMA. Rather, BR and SMIM4 KO C2C12 redistribute UQCC1 signal from COMB to COMA without affecting total UQCC1/2 levels (Figures 3D and S3D). Like BR KO, SMIM4 KO decreased CIII dimer formation (Figure 3D). BN-PAGE of BR KO heart mitochondria confirmed the loss of the COMB complex *in vivo*, but without a redistribution to COMA. This is accompanied by a significant downregulation of total UQCC1 and UQCC2 levels (Figures 3E and S3E), indicating that COMB lacking BR are removed *in vivo* rather than recycled to COMA. Loss of COMB in BR KO was also evident in sucrose gradient fractions of heart mitochondria, where UQCC1 signal was depleted in the COMB fractions in BR KO (Figure S3F). These results demonstrate that BR and SMIM4 are required specifically for the integrity of COMB. In BR KO heart mitochondria, the loss of COMB can be reversed by adeno-associated virus-mediated expression of BR, with a concomitant partial rescue in mature CIII dimer formation (Figure 3F).

Figure 2. BR forms a protein complex with CIII early assembly factors

(A) Analysis of BR containing complexes on BN-PAGEs. Mitochondrial proteins were isolated from mouse hearts and C2C12 myoblasts. Both WT and BR KO mice were littermates sacrificed at around 9 weeks. Expression of BR gRNA #1 (BR g1) was mediated by lentivirus in C2C12 myoblast.

(B) Silver staining of BR interaction partners after co-IP using FLAG tagged BR expressed from mouse hearts by adeno-associated virus (AAV). WT mice of the same litter were sacrificed 4 weeks after AAV injection.

(C) BR interactome as identified by co-IP/MS. Detected proteins were plotted by label-free quantification (LFQ) intensity and folds of enrichment in BR-FLAG IP samples.

(D) Immunoblotting validation of top interaction candidates of BR. BR-FLAG was expressed from mouse hearts by AAV. WT mice of the same litter were sacrificed 4 weeks after AAV injection. 1% of total mitochondria lysate were loaded as input. Non-specific signal was marked by the asterisk.

(E and F) Co-IP of COMB complex subunits by using SMIM4, UQCC1, and C16ORF91 as baits. FLAG-tagged SMIM4, UQCC1, and C16ORF91 were expressed from C2C12 myoblasts.

(G) Mobility of FLAG tagged BR, SMIM4, C16ORF91, and UQCC1 on BN-PAGE. Positions of COMA and COMB complexes were indicated by blue and red arrows, respectively.

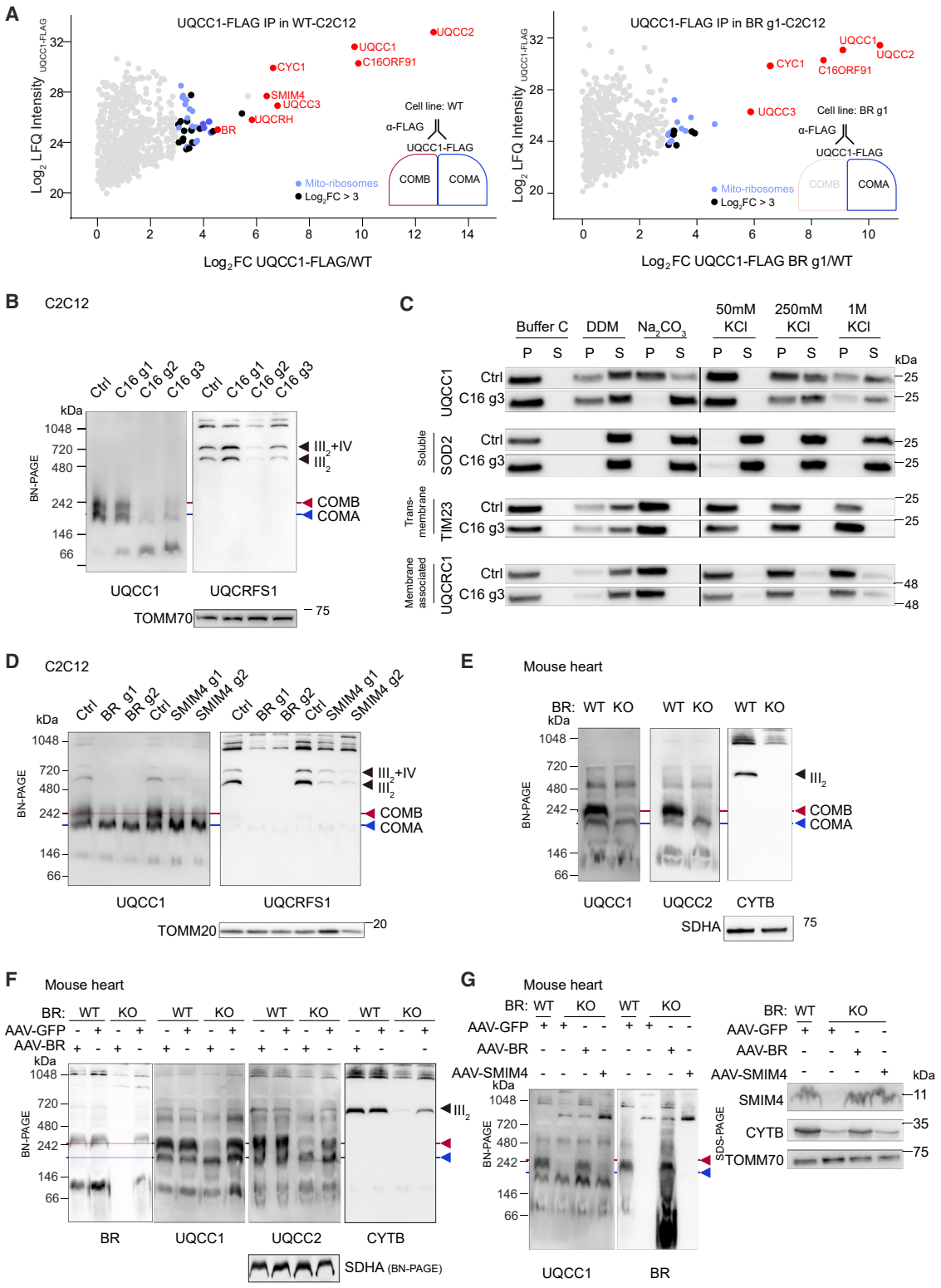

Figure 3. Microproteins are essential for the localization and integrity of COMA and COMB complexes

(A) MS analyses of UQCC1 interacting partners in WT (left) and BR deficient (right) C2C12 myoblast. Detected proteins were plotted by LFQ intensity and folds of enrichment in UQCC1-FLAG IP samples, n = 3 biological replicates.

(legend continued on next page)

We next asked if BR and SMIM4 were redundant, noting that although they have almost no sequence homology in mammals (Figure S3G), in *Drosophila* their homologs are translated from a bicistronic transcript containing two ORFs suggesting that they are paralogs (Bosch et al., 2020). Three lines of evidence indicate that they are not functionally redundant. First, SMIM4 is the most downregulated protein in BR KO mitochondria (Figure 1A). Likewise, SMIM4 KO in C2C12 abolishes BR protein (Figures S3H and S3I), indicating that they are co-dependent. Second, BR and SMIM4 enhance the stability of the other (Figures S3J and 2G), reinforcing their mutual dependence. Furthermore, increased COMB formation is only seen when both BR and SMIM4 are overexpressed (Figure 2G). Last, SMIM4 cannot rescue BR deficiency as measured by COMB complex and total CYTB protein levels (Figure 3G). Rather, BR and SMIM4 function as obligate co-dependent partners in maintaining COMB complexes.

Hence, early CIII assembly in mammals appears to be regulated by two distinct complexes: COMA and COMB that both contain UQCC1/2/C16ORF91 but are distinguished by the absence or presence of obligate partners BR and SMIM4, respectively. Both complexes are bound to the IMM by UQCC4.

UQCC3 defines a distinct COMC complex

In our IP-MS of UQCC1-FLAG, we noted that UQCC3 was co-purified with UQCC1 (Figure 3A), consistent with findings that the yeast homolog UQCC3—Cbp4—functions as a chaperone with yeast UQCC1/2 (Cbp3/6) to monitor CYTB hemylation status. Importantly, this interaction was preserved in BR KO C12C12 (Figure 3A), indicating that UQCC3-UQCC1 interaction is independent of BR. Of note, UQCC3 does not share sequence homology with BR or SMIM4 and are not predicted as paralogs (Figure S4A), although they share the feature of being short peptides.

To clarify whether UQCC3 was a part of COMA or COMB, we performed UQCC3-FLAG IP/MS (Figure 4A) and IP/western blotting (Figure S4B). These analyses demonstrated that the UQCC3-containing complex consists of UQCC1/2/4, but does not include BR/SMIM4. Likewise, BR IP does not recover UQCC3 (Figure S2A). Hence, BR/SMIM4 and UQCC3 independently interact with UQCC1/2/4 but not with each other, suggesting that they are in mutually exclusive complexes. We hypothesized that UQCC3 might belong to an alternative COMB-like complex. Similar to BR/SMIM4, UQCC3 co-migrates with UQCC1/SMIM4/BR in the approximately 240-kDa band corresponding with COMB in 293T cells (Figure 4B). Similar to BR/SMIM4 KO, UQCC3 KO C2C12 mitochondria have decreased levels of the approximately 240-kDa UQCC1 band (Figure 4C), indicating that UQCC3 is required for this COMB-like complex, which we designate as "COMC." Overexpression of BR and SMIM4 in UQCC3 KO C2C12 partially rescues the CIII defect in UQCC3 KO C2C12 (Figure 4C). Hence, we conclude that the approximately 240-kDa complex can be further separated into COMB (BR/SMIM4) and COMC (UQCC3) that are partially redundant but mutually exclusive (Figure 4D). Notably, UQCC3 interacts strongly with CIII core subunits (Figure 4A), while BR (Figure 2C) and UQCC1 (Figure 3A) are not. This suggests that COMC functions downstream of COMB closer to intermediate II (Figure 1E). We next sought to determine the functional roles of these complexes.

COMB and COMC are not required for CYTB translation

We next investigated the roles of COMA, B and C complexes vis-à-vis CYTB synthesis. We first isolated mito-ribosome fractions from HEK293T mitochondria and observed that UQCC1 signal overlapped substantially with proteins of the small and large mito-ribosome subunits (Figure S5A) (mitochondrial small subunit [mtSSU] and mitochondrial large subunit [mtLSU], lanes 4–5) and with monosomes (lanes 7–9). BR comigrated with mtSSU, mtLSU but only marginally with monosomes. In contrast, UQCC3 did not colocalize with mtLSU or monosomes. This suggests that while COMA is ribosome associated, COMB is only weakly associated and COMC is not ribosome associated. This is consistent with IP/MS data showing that UQCC3 does not appreciably interact with mito-ribosome subunits (Figure S4C), while UQCC1 has a wide association (Figure 3A). Consistent with this and with previous findings, ^{35}S-methionine/cysteine (^{35}S-Met/Cys) pulse labeling of nascent mitochondrial proteins in C2C12 cells demonstrated that UQCC1 is required for CYTB translation (Figures 5A and 5B). However, neither BR/SMIM4 (Figures 5A and 5B) nor UQCC3 KO (Figures 5C and S5B) had any effect on nascent CYTB production. We conclude that COMA is required for the earliest step of CYTB biogenesis, i.e., its translation. COMB and C, in contrast, are not directly required for this step and likely functions directly downstream of CYTB translation.

COMB is required for nascent CYTB stabilization

In support of the proximal role of COMB downstream of CYTB translation, BR interacts strongly with nascent CYTB as

(B) Loss of C16ORF91 destabilizes both COMB and COMA. Mitochondria of cell lines expressing three C16ORF91 gRNAs (C16 g1–3) were analyzed by BN-PAGE and immunoblotting. TOMM70 was probed as loading control in SDS-PAGE.

(C) C16ORF91 is required for the membrane association of UQCC1. Mitochondrial proteins of WT and C16ORF91-deficient cells were fractioned in insoluble (pellet [P]) and soluble (S) fractions under the indicted conditions.

(D) BR KO destabilizes the COMB complex. Mitochondria of cell lines expressing three BR or SMIM4 gRNAs (g1–3) were analyzed by BN-PAGE and immunoblotting. TOMM20 was probed as loading control in SDS-PAGE.

(E) Experiment as shown in (D), mitochondria were isolated from hearts of paired WT and BR KO mouse littermates at approximately 9 weeks. SDHA was probed as loading control in SDS-PAGE.

(F) Rescuing of BR KO by adeno-associated virus (AAV)-mediated BR expression in mouse hearts. Both WT and KO mice were littermates sacrificed 4 weeks after AAV injection. Heart mitochondria were analyzed by BN-PAGE and immunoblotting. CIII dimer, COMA, and COMB complexes were indicated by black, blue, and red arrows, respectively.

(G) BN-PAGE (left) and SDS-PAGE (right) analysis of mitochondrial complexes in BR KO infected with AAVs expressing GFP, BR, or SMIM4 proteins. Both WT and KO mice were littermates sacrificed 4 weeks after AAV injection. COMA and COMB complexes are indicated by blue and red arrows, respectively.

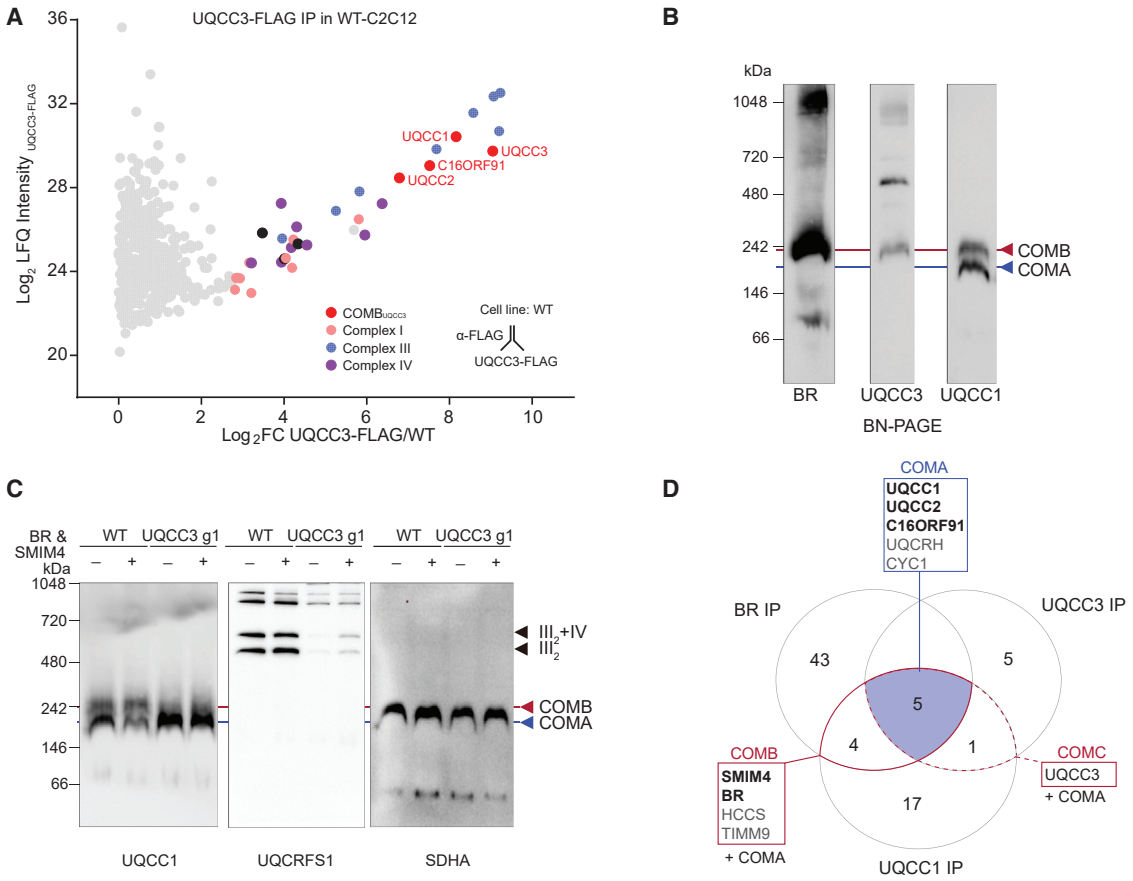

Figure 4. UQCC3 defines a distinct COMC complex

(A) Co-IP/MS in C2C12 myoblasts determine UQCC3 interactome. Subunits of COMC and RC complexes are marked by indicated colors. Detected proteins were plotted by LFQ intensity and folds of enrichment in UQCC3-FLAG IP samples, n = 3 biological replicates.

(B) Mobility of BR, UQCC1, and UQCC3 is visualized in BN-PAGE. Mitochondrial proteins were isolated from WT HEK293T cells.

(C) Partial rescue of UQCC3 deficiency induced CIII defects by BR and SMIM4 over-expression in C2C12 cells.

(D) Venn diagram showing the shared and distinct subunits of COMA, COMB, and COMC that were revealed by co-IP of BR, UQCC1, and UQCC3. Highly enriched proteins (log_2fold change > 3 and -log_{10}p value >2) were included for this analysis.

determined by radioactive co-IP (Figure 5D). We next performed a ^{35}S-Met/Cys pulse-chase experiment to interrogate the stability of nascent CYTB in the absence of COMB or COMC. This analysis revealed that CYTB in BR and SMIM4 KO (Figures 5E and S5C) and UQCC3 KO (Figures 5F and S5D) are more rapidly degraded in KO cells relative to WT cells, suggesting a loss of CYTB stability after translation in the absence of COMB or COMC. CYTB translation undergoes hemylation and insertion into the IMM before association with other intermediate II subunits UQCRQ and UQCRB. By performing sodium carbonate extraction of membrane proteins after a 1-h ^{35}S-Met/Cys pulse, we found that BR KO had a 20% decrease of total nascent CYTB found in the membrane compared with WT, while UQCC3 KO had no such defect (Figures 5G and S5E). Hence COMB but not COMC plays a role in promoting nascent CYTB membrane incorporation. Downstream of membrane insertion, there was a significant decrease in the association of nascent CYTB with intermediate II subunit UQCRQ in BR KO C2C12 (Figure 5H), indicating a decrease in early CIII assembly secondary to the defect in CYTB biogenesis. That UQCC3 KO C2C12 have normal CYTB membrane insertion suggests functional specialization of COMB. COMC, according to the known role of Cbp4 in cytb hemylation in yeast (Hildenbeutel et al., 2014), might be instead involved in the further maturation of CYTB downstream of membrane insertion. To confirm the role of COMC in mammalian CIII early assembly, we quantified the heme levels incorporated into total CYTB captured by IP in C2C12 cells lacking BR (COMB), UQCC3 (COMC), or the first nuclear-encoded subunit UQCRQ (Figure 5I), normalized to CYTB levels in the eluate (Figure S5H). As expected, UQCC3 (COMC) mutants had a 25% decrease in CYTB-associated heme levels, consistent with its known function in yeast. The decrease is modest; our approach does not distinguish nascent CYTB from the total CYTB protein pool. BR (COMB) KO cells also displayed a modest decrease in heme levels, suggesting that a stall in the preceding membrane insertion step also negatively impacts hemylation. Surprisingly, UQCRQ KO cells had a more than two-fold increase in heme levels, indicating that when CYTB association with

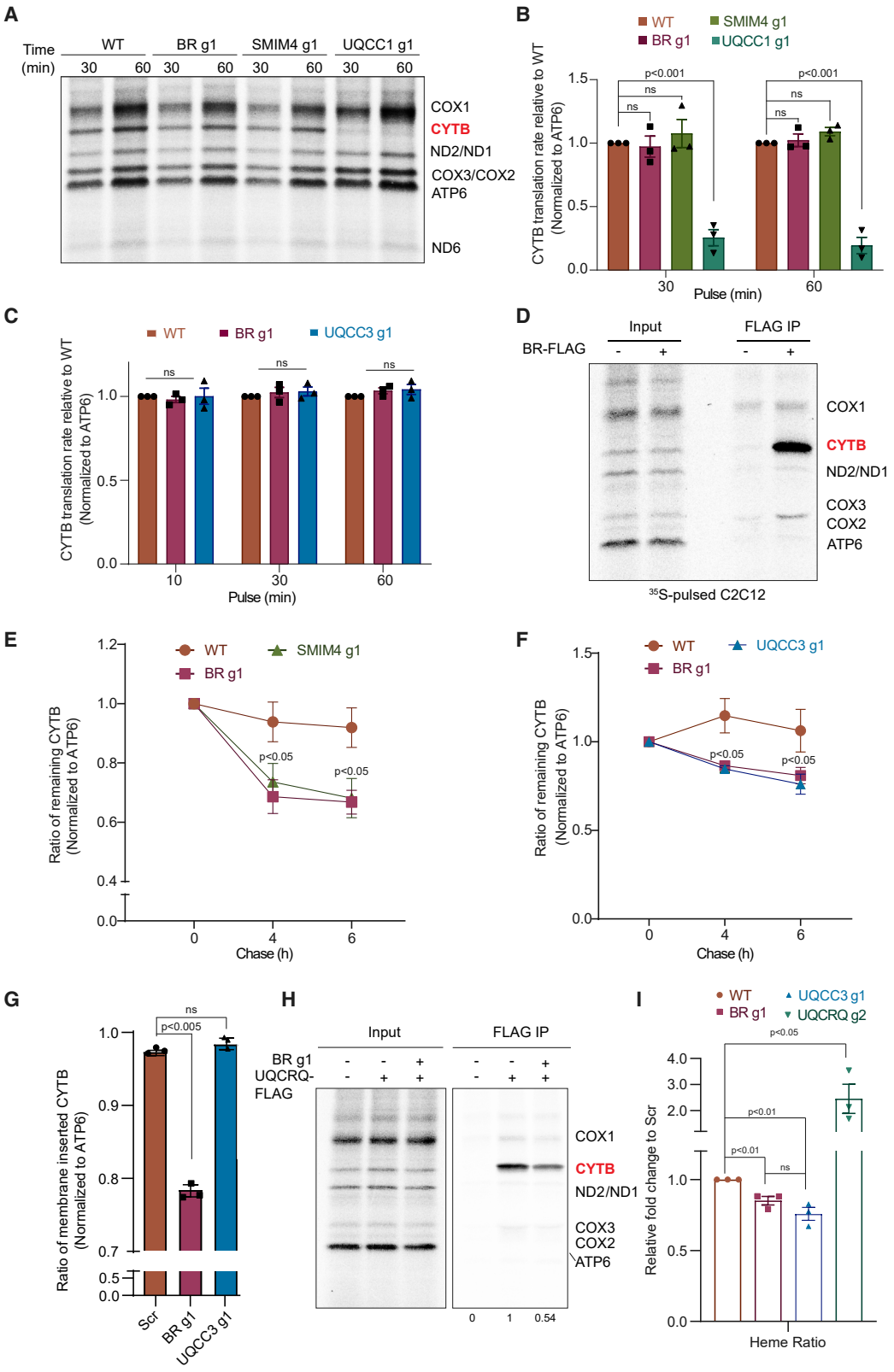

(legend on next page)

nuclear-encoded subunits is impeded, its increased association with COMB/C facilitates hyper-hemylation. Hence, our studies confirm previous findings in yeast that UQCC3 is required for CYTB hemylation and that there might be redundancy between COMB and COMC vis-à-vis CYTB hemylation.

Of note, we also did not detect any interaction or changes in the levels of OXA1L—the known membrane insertase for IMM proteins (Hell et al., 2001; Keil et al., 2012)—with COMB (Figure S5F). Similarly, membrane association of UQCC1 (representing COMA and COMB) did not change in BR KO mitochondria as ascertained by differential salt extraction assays (Figure S5G), suggesting that BR does not promote CYTB insertion by anchoring COMB to the IMM.

COMB activity coordinates CIII biogenesis with metabolic cues

CIII occupies a central position in the ETC as the common acceptor of electrons from multiple catabolic pathways generating NADH and $FADH_2$. CIII levels can therefore be modulated to change the overall activity and output of the respiratory chain. Consistent with a positive role for COMB in CIII biogenesis, overexpression of SMIM4 and BR together in C2C12 cells increased the steady-state levels of CIII in dimers and supercomplexes (Figure S6A). We therefore hypothesized that SEPs like BR and SMIM4 can respond dynamically to metabolic cues to regulate ETC biogenesis by changing levels of assembly factors. Previously, we found that BR is induced by AICAR—an agonist of the nutrient-sensing AMPK pathway—along with OXPHOS components (Zhang et al., 2020). Like the AMPK pathway, the PI3K/AKT pathway is known to stimulate mitochondrial biogenesis in response to nutrients and insulin/insulin growth factor (IGF)-1 (Lyons et al., 2017; Riis et al., 2020). Indeed, similar to AICAR, insulin/IGF treatment of C2C12 cells increased the BR level (Figure 6A) and the COMB/COMA ratio (Figure S6B) and increased the formation of mature CIII dimers (Figure S6B). An increase in CIII biogenesis—as represented by the late incorporating subunit UQCRFS1—was dependent on BR, as BR KO cells did not upregulate CIII in response to either insulin (Figures 6B and 6D) or AICAR (Figures 6C and S6C) to the same extent as WT. Consequently, the increase in oxygen consumption in response to insulin is attenuated in BR KO cells (Figure 6D). During starvation and cold stress, cells also induce compensatory mitochondrial biogenesis to maintain energy output (Latorre-Muro et al., 2021). In line with AMPK-induced expression of BR, cold stress (Figures 6E and S6D) and glucose starvation (Figures 6F and S6E) also induced expression of BR and ETC proteins. Again, cold- and starvation-induced increases in CIII biogenesis were dampened in BR KO cells. Altogether, these data show that BR and thus COMB are required to safeguard CIII levels and ETC homeostasis in response to energy perturbation and metabolic stress.

COMB is required for nuclear-mitochondrial coordination of CIII biogenesis

During CIV biogenesis, the MITRAC complex enables mitochondrial translational plasticity by tuning *COX1* mRNA translation according to the availability of nuclear encoded COX4 (Richter-Dennerlein et al., 2016). In yeast, Cbp3/4/6 governs feedback regulation of Cyt*b* translation by dissociating from nascent Cyt*b* upon Qcr8 association, and recycling back to the mito-ribosome for further rounds of Cyt*b* translation (Gruschke et al., 2012). Any delay in Qcr8 association causes Cbp3/4/6 to remain bound to Cyt*b*, unavailable for new rounds of Cyt*b* translation (Hildenbeutel et al., 2014). We hypothesized that COMB is the mammalian counterpart of the MITRAC complex for CIII assembly and coordinates CYTB translation with availability of nuclear-encoded CIII subunits. To test this hypothesis, we deleted UQCRQ (Figure S7A), the mammalian homologue of Qcr8, to mimic a loss of import of nuclear CIII subunits. UQCRQ KO significantly decreased CYTB translation (Figure 7A) and led to an accumulation of COMB but not COMA (Figure 7B), along with an increase in BR levels (Figure 7C). Depletion of COMB by BR KO in UQCRQ KO cells did not affect CYTB translation further (Figures 7D and S7B), but further decreased the post-translational stability of nascent CYTB (Figures 7E and S7C). Consequently, BR/UQCRQ double KO (DKO) had a greater loss of mature CIII compared with UQCRQ KO (Figure 7F). These data indicate that when nuclear-mitochondrial coordination is

Figure 5. COMB is required for the stabilization of nascent CYTB but not its translation

(A) CYTB translation rate is not affected by COMB depletion. C2C12 cells were pulse labeled for 30 and 60 min with ^{35}S-labeled methionine and cysteine (^{35}S-Met and Cys) in the presence of emetine.

(B) Quantification of CYTB translation rates shown in (A). ATP6, an CV subunit independent of CIII assembly, was used for the normalization. Data are represented as mean ± standard error of the mean, n = 3 biological replicates. p values are from two-tailed unpaired *t* tests.

(C) Similar to (B), CYTB translation rates were determined in BR and UQCC3 deficient C2C12 cells. Data are represented as mean ± standard error of the mean, n = 3 biological replicates. p values are from two-tailed unpaired *t* test. A representative phosphor image is shown in Figure S5B.

(D) BR specifically binds to newly synthesized CYTB. Cells expressing BR-FLAG were labeled with ^{35}S-Met & Cys for 2h in the presence of cycloheximide. BR-FLAG and its interaction partners were purified under a native condition before SDS-PAGE.

(E) Newly synthesized CYTB is destabilized upon loss of BR and SMIM4. Proteins were isolated at the indicated chase time points after a 2h pulse labeling in the presence of cycloheximide. Data are represented as mean ± standard error of the mean, n = 3 biological replicates. p values are from two-tailed unpaired *t* test. A representative phosphor image is shown in Figure S5C.

(F) Similar to (E), CYTB stability was measured in BR and UQCC3 deficient cells. Data are represented as mean ± standard error of the mean, n = 3 biological replicates. p values are from two-tailed unpaired *t* test. Representative phosphor image is shown in Figure S5D.

(G) Membrane association of newly translated CYTB was examined by alkaline extraction assay. Representative phosphor image is shown as Figure S5E. Data are represented as mean ± standard error of the mean, n = 3 biological replicates. p values are from two-tailed unpaired *t* test.

(H) BR deficiency weakens the interaction between CYTB and CIII early assembly subunit UQCRQ. UQCRQ-FLAG expressing from WT and BR deficient cells was purified after ^{35}S radioisotope labeling in the presence of cycloheximide. Relative abundance of co-purified CYTB was indicated.

(I) C2C12 cells lacking UQCC3 fail to hemylate CYTB. Normalized abundance of CTYB bound heme was quantified by a colorimetric reaction after CYTB IP (Figure S5H). Data are represented as mean ± standard error of the mean, n = 3 biological replicates. p values are from two-tailed unpaired *t* test.

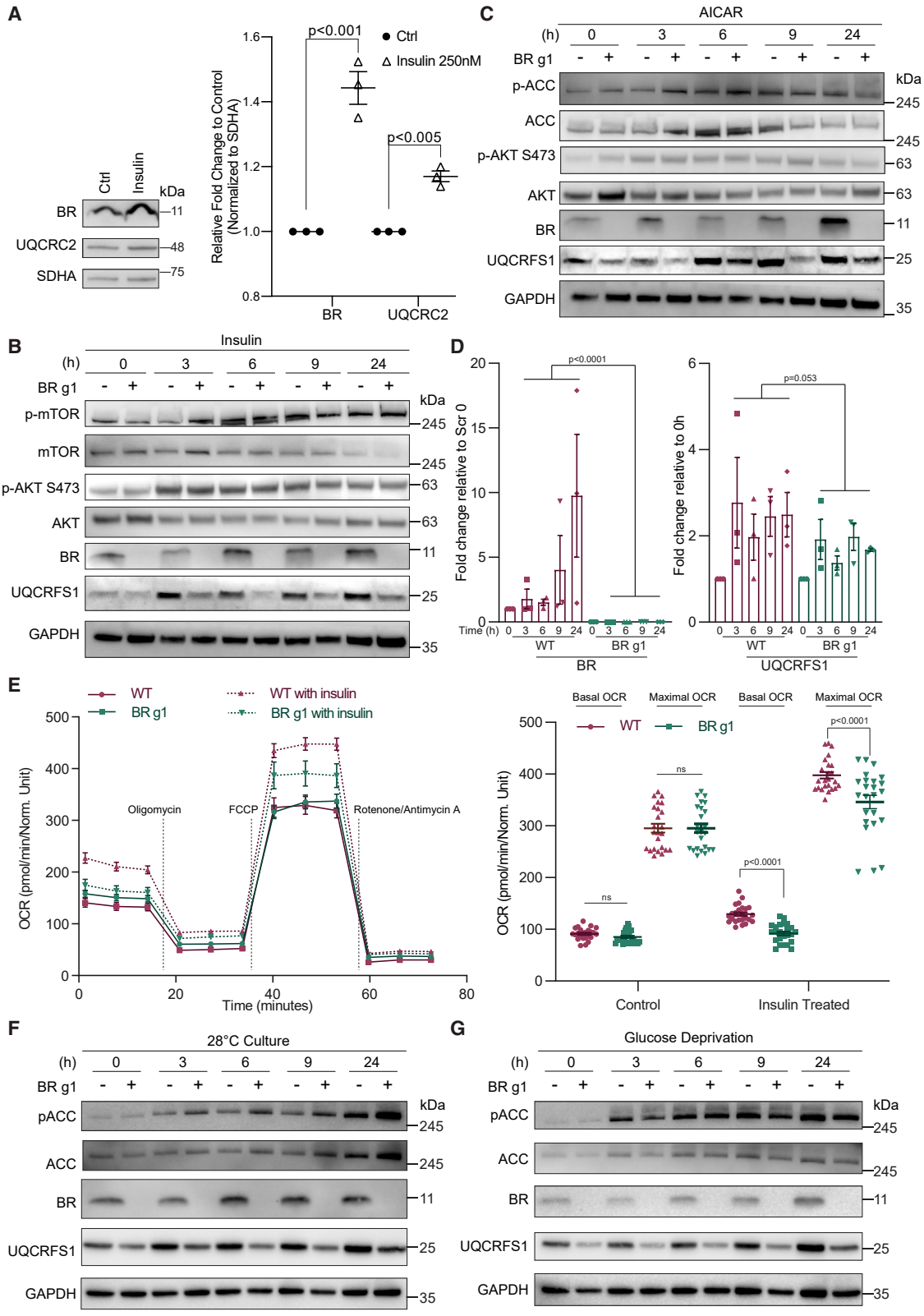

(legend on next page)

affected, BR (COMB) is required for preserving residual CIII biogenesis and maintaining cell viability.

Last, we asked if the early steps of CYTB biogenesis and the COM complexes are involved in sensing mitochondrial stress. Mitochondrial stress induced by poisons such as oligomycin and uncoupling agents such as FCCP activate an integrated stress response through the OMA1-Dele1-HRI pathway (Fessler et al., 2020; Guo et al., 2020) that culminates in ATF4 induction. ATF4 in turn activates a transcriptional program aimed at proteostasis and survival, enabling adaptive mitochondrial homeostasis until the stress is resolved (Pakos-Zebrucka et al., 2016). We found that, at basal state, UQCRQ KO cells induced ATF4 (Figure S7D), indicative of mitochondrial stress and consistent with the observed respiratory defect (Figure 7G). Surprisingly, BR KO attenuated this increase in ATF4 induction in UQCRQ KO (Figure S7D), suggesting that COMB contributes to stress sensing. Since basal levels of ATF4 were low, we treated the cells with oligomycin, a potent inducer of ATF4. Under such circumstances, we found that BR KO indeed had decreased ATF4 protein and other integrated stress response (ISR) gene induction, and completely abrogated ATF4 protein and ISR gene induction observed in UQCRQ KO cells (Figures S7D and S7E). Notably, UQCRQ KO cells have dramatically reduced ability to induce ATF4 upon oligomycin challenge, suggesting the first meeting point of mitochondrial and nuclear CIII subunits is also required for effective stress sensing. Consistent with the loss of stress sensing, DKO cells had markedly decreased respiration (Figure 7G) and cell viability as measured by competitive growth with GFP-labelled WT cells in galactose-containing media (Figure 7H).

Taken together, our results indicate that CYTB biogenesis—including its translation and post-translational maturation—is a critical checkpoint for monitoring the overall quality of OXPHOS. This process is curated by 3 complexes with distinct roles—COMA, COMB, and COMC. COMB responds dynamically to nutritional status and mitochondrial stress and is critical for ETC homeostasis and cell viability under conditions that affect OXPHOS integrity.

DISCUSSION

In this study, we demonstrate that BR and other hitherto uncharacterized mito-SEPs SMIM4 and C16ORF91 mediate the first step of CIII assembly—CYTB biogenesis. Synthesis of mammalian CYTB in the mitochondrial matrix relies on three complexes, collectively termed the "co-ordinator of mitochondria CYTB" or "COM" complexes which are localized to the IMM by C16ORF91 (herein named UQCC4). Ribosome-associated COMA comprising UQCC1/2/4 first activates CYTB translation. COMB comprising SMIM4/BR/UQCC1/2/4 subsequently stabilizes nascent CYTB and promotes its membrane insertion. After COMB-mediated membrane insertion, nascent CYTB is passed on to COMC, which comprises UQCC1/2/3/4 and mediates CYTB hemylation and association with the first nuclear-encoded CIII subunit UQCRQ. COMB protein levels are regulated by signals of energy and stress, adapting ETC output to metabolic status. Signals that activate mitochondrial biogenesis—insulin and AMPK agonist AICAR, as well as nutrient deprivation and temperature stress—increase COMB levels by upregulating BR. Consequently, *Br* KO cells fail to adaptively increase CIII biogenesis in response to these signals. Furthermore, by chaperoning excess CYTB when downstream nuclear-encoded interacting subunit UQCRQ is limiting, COMB potentiates the activation of a protective retrograde mitochondrial stress response involving ATF4. As such, COMB provides a buffering mechanism to prevent ETC collapse when mitochondrial-nuclear genome coordination is disrupted. Our study delineates the sequence of early events required for successful CIII assembly in mammals and demonstrate that CYTB synthesis is a key regulatory node for coordinating ETC synthesis with metabolic cues and stress.

The mechanisms underlying mammalian CIII assembly are unclear and assumed to follow the model informed by yeast studies. Here, we have characterized in detail the complexes that undergird early mammalian CIII assembly beginning at CYTB translation, revealing similarities and notable differences from yeast. CIII assembly in yeast begins with the translation of *COB* mRNA from the mitochondrial genome. *COB* mRNA is translated to produce cytochrome *b* (Cyt*b*) under the control of two sets of regulators—Cbs1, Cbs2, Cbp1, and the Cbp3/Cbp6 complex (García-Guerrero et al., 2018; Gruschke et al., 2011, 2012). Cbp3/Cbp6 competes with Cbs1 at the mito-ribosome exit tunnel to stimulate Cyt*b* translation (Gruschke et al., 2011, 2012; Salvatori et al., 2020). After translation, Cbp3/Cbp6 remains associated with Cyt*b* to assist its hemylation, which is completed upon binding to Cbp4 (yeast homologue for vertebrate UQCC3) (Hildenbeutel et al., 2014). COMA is thus the mammalian equivalent of Cbp3/6 and aids CYTB translation, presumably by promoting the emergence of nascent CYTB from the exit tunnel of the ribosome (Gruschke et al., 2011). Nascent CYTB then associates with the COMB, which

Figure 6. COMB activity coordinates CIII biogenesis with metabolic cues

(A) Insulin induces the expression of BR. Protein levels of BR and UQCRC2 were analyzed by western blotting after treating C2C12 cell with 250 nM insulin. Data are mean ± standard error of the mean, n = 3 biological replicates. p values are from two-tailed unpaired *t* tests.

(B) Time course analysis of BR and UQCRFS1 level after insulin treatment in WT and BR deficient C2C12 cells. GAPDH normalized abundance of BR and UQCRFS1 in WT and BR g1 were quantified and normalized to their abundance at 0 h.

(C) Similar to (B), cells were treated with 500 μM AMPK activator AICAR.

(D) Statistical analysis of BR and UQCRFS1 levels shown in (B). Data are represented as mean ± standard error of the mean, n = 3 biological replicates. p values are from two-tailed unpaired t tests.

(E) BR KO is defective in boosting mitochondria respiration capacity following insulin treatment. Basal and maximal (FCCP) oxygen consumption rates (OCR) were measured and quantified. Data are represented as mean ± standard error of the mean, n = 16 technical replicates. p values are from two-tailed unpaired t tests.

(F) Similar to (B), cells were cultured at 28°C with 5% CO_2.

(G) Similar to (B), cells were cultured in DMEM glucose-free media.

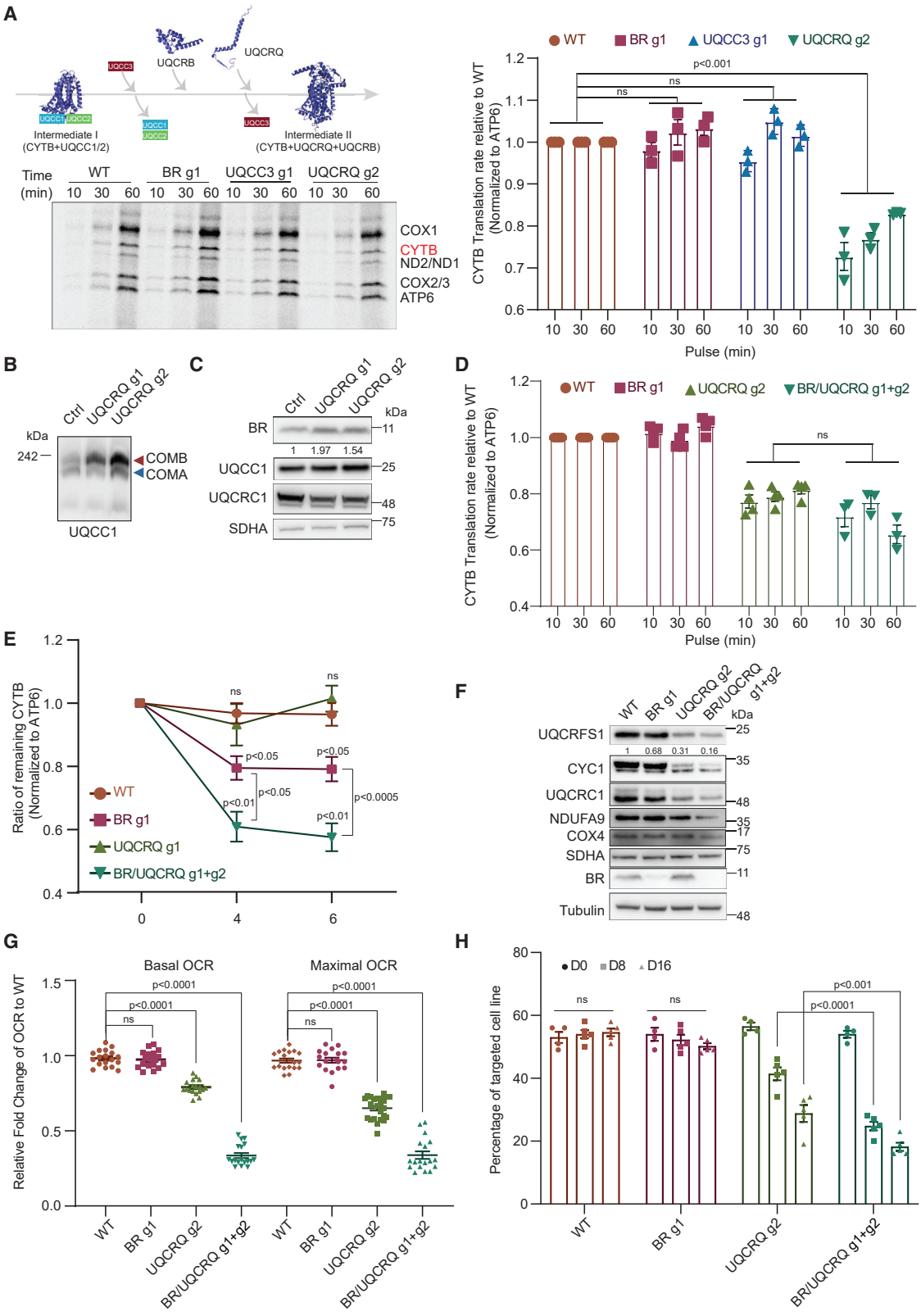

(legend on next page)

is not present in yeast, to aid in its post-translational stabilization and promote membrane insertion by serving as a chaperone. Mammalian CYTB biogenesis therefore uses three additional proteins that arose during vertebrate evolution—BR, SMIM4, and UQCC4. All three proteins share the property of being mito-SEPs—small proteins that are nuclear encoded and imported into the mitochondria. Notably, all three proteins have single-pass TMDs. UQCC4 tethers the UQCC1/2 complexes to the inner membrane as these proteins shuttle from the ribosome through to membrane insertion, hemylation, and association with UQCRQ. The additional membrane anchors provided by BR and SMIM4 may be crucial for the post-translational stabilization of nascent CYTB, and it is tantalizing to speculate that the TMDs of BR/SMIM4/UQCC4 together form a conduit that is required for membrane insertion of CYTB, independent of known chaperones or insertases. We postulate that these mito-SEPs involved in CYTB biogenesis arose during vertebrate evolution driven by the need for increased robustness against mitochondrial stress and energy perturbation in multicellular organisms.

COMA and COMB form a two-module system that provide a fail-safe mechanism for tuning the levels of CYTB availability. Similarly, while the post-translational maturation of Cytb relies only on Cbp3/4/6—the equivalent of COMC—the mammalian process requires an additional COMB to precede COMC. Because COMB levels respond dynamically to external metabolic cues, the kinetics of CYTB maturation can be finetuned to match and respond to prevailing nutrient and energy availability. Similarly, when nuclear-encoded CIII subunits are limiting, COMB plays an essential chaperoning function to keep CYTB in an assembly-competent stable state until such subunits are available again (Hildenbeutel et al., 2014). This is reminiscent of the functions of mtHsp70—which holds Cox4 in a reserve complex when CIV assembly is stalled (Böttinger et al., 2013)—and the MITRAC complex, which forms an assembly intermediate with nascent Cox1 when Cox4 is limited (Richter-Dennerlein et al., 2016). COMB is, therefore, part of the general mechanism to enable translational plasticity and maintain nuclear-mitochondria coordination during times of stress. Such mechanisms allow cells to rapidly adapt to changing fuel availability and growth environment. In this respect, it is tempting to speculate that the small size of the mito-SEPs in COMB complexes enable them to be rapidly synthesized and efficiently imported into the mitochondria during energy stress. As such, enhancing the expression of such mito-SEPs might be a potential therapeutic strategy for improving the bioenergetic performance of mitochondria in disease settings of mitochondrial dysfunction or insufficiency.

Limitations of the study

At present, our data do not distinguish between the scenario where CYTB shuttles from COMA to COMB from an alternate model where COMA-CYTB recruits BR/SMIM4 to form COMB-CYTB and further work will be required to resolve these fine differences. Although our data suggest that COMB and COMC are functionally distinct and act sequentially, BR/SMIM4 seem to partially compensate for the absence of UQCC3, suggesting the ability for functional redundancy when the need arises. Studies will be required to further clarify the relationship between these two complexes.

STAR★METHODS

Detailed methods are provided in the online version of this paper and include the following:

- KEY RESOURCES TABLE
- RESOURCE AVAILABILITY
  - Lead contact
  - Materials availability
  - Data and code availability
- EXPERIMENTAL MODEL AND SUBJECT DETAILS
  - Animals
  - Cell lines
- METHOD DETAILS
  - Cell culture
  - Plasmid construction
  - BR KO mouse generation and genotyping
  - Mouse treadmill exercise
  - Mitochondria isolation
  - Mouse heart mitochondrial proteome analysis
  - SDS-PAGE and immunoblotting
  - Native PAGE
  - Gene editing by CRISPR

Figure 7. COMB is required for nuclear-mitochondrial coordination of CIII biogenesis

(A) UQCRQ mutant is defective in CYTB translation. C2C12 cells of indicated genotypes were pulse-labelled with ^{35}S-Met and Cys for 10, 30 and 60 min in the presence of emetine. Data are represented as mean ± standard error of the mean, n = 3 biological replicates. p values are from one-way ANOVA test. The cartoon (top) shows the schematic early assembly of CIII.

(B) UQCC1 is sequestered in COMB under the loss of UQCRQ. Mobility of UQCC1 was analyzed by BN-PAGE in WT and UQCRQ deficient C2C12 cells.

(C) UQCRQ deficient cells have a higher BR level. C2C12 cell lysates of indicated genotypes were used for immunoblotting.

(D) Concurrent loss of BR and UQCRQ does not impair CYTB translation further. Similar to (A), a representative image is shown as Figure S7B. Data are represented as mean ± standard error of the mean, n = 4 biological replicates (except n = 3 for BR/UQCRQ g1+g2). p values are one-way ANOVA test.

(E) Concurrent loss of BR and UQCRQ further exacerbates the stability of CYTB. Protein stability of nascent CYTB was followed in the course of 6 h after a 2-h labeling. A representative image is shown as Figure S7C. Data are represented as mean ± standard error of the mean, n = 3 biological replicates. p values are from two-tailed unpaired *t* tests.

(F) Level of CIII subunits was determined in C2C12 cells with indicated genotypes by SDS-PAGE. Numbers under SDS-PAGE are quantifications of band intensity normalized to Tubulin.

(G) UQCRQ deficient C2C12 cells show defects in basal and maximal respiration. p values are from two-tailed unpaired *t* tests. OCR, oxygen consumption rate.

(H) UQCRQ deficient C2C12 cells show growth defects using GFP competitive assay. Data are represented as mean ± standard error of the mean, n = 3 biological replicates. p values are from two-tailed unpaired *t* tests.

- Virus production and transduction
- AAV production and infection
- Protein co-immunoprecipitation and mass spectrometry
- Polysome profiling and ribosome association
- Sucrose gradient fractionation
- Mitochondria membrane fractionation assay
- Protease sensitivity assay
- Membrane association assay
- Mitochondrial translation metabolic labeling
- Seahorse assay
- Citrate synthase activity assay
- GFP competitive assay
- Quantitative PCR assay

- QUANTIFICATION AND STATISTICAL ANALYSIS

SUPPLEMENTAL INFORMATION

Supplemental information can be found online at https://doi.org/10.1016/j.celrep.2022.111204.

ACKNOWLEDGMENTS

We thank Shang Li (Duke-NUS) for the kind provision of lentiviral constructs and advice for Crispr/Cas9-mediated knockout generation, Ann-Marie Chacko (Duke-NUS) for the supervision of radioisotope-related work, and Xu Dan (Duke-NUS) for generating the Br mouse knockout. This work was funded by NRF-NRFF2017-05 and HHMI IRSP 55008732 awarded to L.H., and by RECA RECA(Pilot)/2019/0045 awarded to L.H. and D.M. S.Z. is supported by a KTP postdoctoral fellowship. L.S. is supported by OF-IRG, MOH-000954, and MOH-000379. D.S. is supported by grants from the Australian National Health and Medical Research Council (NHMRC Project Grant 1140906 and NHMRC Fellowships 1140851). We acknowledge the support of the Mito Foundation (Australia) for the provision of mass spectrometry instrumentation through the large equipment grant support scheme. We thank the Bio21 Mass Spectrometry and Proteomics Facility (MMSPF) for provision of instrumentation, training, and technical support.

AUTHOR CONTRIBUTIONS

C.L., S.Z., and L.H. conceived this work; C.L. and S.Z. performed all experiments with collaborative help from D.R., D.T., and D.S. (mass spectrometry); S.B. and R.L. (BR animal husbandry); J.N. for polysome analysis. L.S. generated the BR KO animals used in the study. D.S. and D.R. performed all mass spectrometry analyses. L.H., C.L., and S.Z. wrote the manuscript.

DECLARATION OF INTERESTS

The authors declare no competing interests.

Received: January 16, 2022
Revised: May 25, 2022
Accepted: July 21, 2022
Published: August 16, 2022

REFERENCES

Acìn-Pérez, R., Bayona-Bafaluy, M.P., Fernández-Silva, P., Moreno-Loshuertos, R., Pérez-Martos, A., Bruno, C., Moraes, C.T., and Enrìquez, J.A. (2004). Respiratory complex III is required to maintain complex I in mammalian mitochondria. Mol. Cell *13*, 805–815. https://doi.org/10.1016/s1097-2765(04)00124-8.

Acín-Pérez, R., Fernández-Silva, P., Peleato, M.L., Pérez-Martos, A., and Enriquez, J.A. (2008). Respiratory active mitochondrial supercomplexes. Mol. Cell *32*, 529–539. https://doi.org/10.1016/j.molcel.2008.10.021.

Atkinson, A., Khalimonchuk, O., Smith, P., Sabic, H., Eide, D., and Winge, D.R. (2010). Mzm1 influences a labile pool of mitochondrial zinc important for respiratory function. J. Biol. Chem. *285*, 19450–19459. https://doi.org/10.1074/jbc.m110.109793.

Atkinson, A., Smith, P., Fox, J.L., Cui, T.-Z., Khalimonchuk, O., and Winge, D.R. (2011). The LYR protein Mzm1 functions in the insertion of the Rieske Fe/S protein in yeast mitochondria. Mol. Cell Biol. *31*, 3988–3996. https://doi.org/10.1128/mcb.05673-11.

Balsa, E., Soustek, M.S., Thomas, A., Cogliati, S., García-Poyatos, C., Martín-García, E., Jedrychowski, M., Gygi, S.P., Enriquez, J.A., and Puigserver, P. (2019). ER and nutrient stress promote assembly of respiratory chain supercomplexes through the PERK-eIF2α Axis. Mol. Cell *74*, 877–890.e6. https://doi.org/10.1016/j.molcel.2019.03.031.

Bosch, J.A., Ugur, B., Pichardo-Casas, I., Rabasco, J., Escobedo, F., Zuo, Z., Brown, B., Celniker, S., Sinclair, D., Bellen, H., et al. (2020). Two neuronal peptides encoded from a single transcript regulate mitochondrial function in Drosophila. Preprint at bioRxiv. https://doi.org/10.1101/2020.07.01.182485.

Böttinger, L., Guiard, B., Oeljeklaus, S., Kulawiak, B., Zufall, N., Wiedemann, N., Warscheid, B., van der Laan, M., and Becker, T. (2013). A complex of Cox4 and mitochondrial Hsp70 plays an important role in the assembly of the cytochrome c oxidase. Mol. Biol. Cell *24*, 2609–2619. https://doi.org/10.1091/mbc.e13-02-0106.

Calvo, S.E., Clauser, K.R., and Mootha, V.K. (2015). MitoCarta2.0: an updated inventory of mammalian mitochondrial proteins. Nucleic Acids Res. *44*, D1251–D1257. https://doi.org/10.1093/nar/gkv1003.

Cantó, C., and Auwerx, J. (2009). PGC-1α, SIRT1 and AMPK, an energy sensing network that controls energy expenditure. Curr. Opin. Lipidol. *20*, 98–105. https://doi.org/10.1097/mol.0b013e328328d0a4.

Chomyn, A. (1996). Mitochondrial biogenesis and genetics Part B. Methods Enzymol. *264*, 197–211. https://doi.org/10.1016/s0076-6879(96)64020-8.

Cox, J., and Mann, M. (2008). MaxQuant enables high peptide identification rates, individualized p.p.b.-range mass accuracies and proteome-wide protein quantification. Nat. Biotechnol. *26*, 1367–1372. https://doi.org/10.1038/nbt.1511.

Crivellone, M.D., Wu, M.A., and Tzagoloff, A. (1988). Assembly of the mitochondrial membrane system. Analysis of structural mutants of the yeast coenzyme QH2-cytochrome c reductase complex. J. Biol. Chem. *263*, 14323–14333. https://doi.org/10.1016/s0021-9258(18)68224-9.

Cui, T.-Z., Smith, P.M., Fox, J.L., Khalimonchuk, O., and Winge, D.R. (2012). Late-stage maturation of the Rieske Fe/S protein: Mzm1 stabilizes Rip1 but does not facilitate its translocation by the AAA ATPase Bcs1. Mol. Cell Biol. *32*, 4400–4409. https://doi.org/10.1128/mcb.00441-12.

Diaz, F., Enríquez, J.A., and Moraes, C.T. (2012). Cells lacking Rieske iron-sulfur protein have a reactive oxygen species-associated decrease in respiratory complexes I and IV. Mol. Cell Biol. *32*, 415–429. https://doi.org/10.1128/mcb.06051-11.

Fernández-Vizarra, E., Ferrín, G., Pérez-Martos, A., Fernández-Silva, P., Zeviani, M., and Enríquez, J.A. (2010). Isolation of mitochondria for biogenetical studies: an update. Mitochondrion *10*, 253–262. https://doi.org/10.1016/j.mito.2009.12.148.

Fessler, E., Eckl, E.-M., Schmitt, S., Mancilla, I.A., Meyer-Bender, M.F., Hanf, M., Philippou-Massier, J., Krebs, S., Zischka, H., and Jae, L.T. (2020). A pathway coordinated by DELE1 relays mitochondrial stress to the cytosol. Nature *579*, 433–437. https://doi.org/10.1038/s41586-020-2076-4.

García-Guerrero, A.E., Camacho-Villasana, Y., Zamudio-Ochoa, A., Winge, D.R., and Pérez-Martínez, X. (2018). Cbp3 and Cbp6 are dispensable for synthesis regulation of cytochrome b in yeast mitochondria. J. Biol. Chem. *293*, 5585–5599. https://doi.org/10.1074/jbc.ra117.000547.

Ghezzi, D., Arzuffi, P., Zordan, M., Da Re, C., Lamperti, C., Benna, C., D'Adamo, P., Diodato, D., Costa, R., Mariotti, C., et al. (2011). Mutations in

TTC19 cause mitochondrial complex III deficiency and neurological impairment in humans and flies. Nat. Genet. *43*, 259–263. https://doi.org/10.1038/ng.761.

Gruschke, S., Kehrein, K., Römpler, K., Gröne, K., Israel, L., Imhof, A., Herrmann, J.M., and Ott, M. (2011). Cbp3-Cbp6 interacts with the yeast mitochondrial ribosomal tunnel exit and promotes cytochrome b synthesis and assembly. J. Cell Biol. *193*, 1101–1114. https://doi.org/10.1083/jcb.201103132.

Gruschke, S., Römpler, K., Hildenbeutel, M., Kehrein, K., Kühl, I., Bonnefoy, N., and Ott, M. (2012). The Cbp3-Cbp6 complex coordinates cytochrome b synthesis with bc1 complex assembly in yeast mitochondria. J. Cell Biol. *199*, 137–150. https://doi.org/10.1083/jcb.201206040.

Guo, X., Aviles, G., Liu, Y., Tian, R., Unger, B.A., Lin, Y.H.T., Wiita, A.P., Xu, K., Correia, M.A., and Kampmann, M. (2020). Mitochondrial stress is relayed to the cytosol by an OMA1–DELE1–HRI pathway. Nature *579*, 427–432. https://doi.org/10.1038/s41586-020-2078-2.

Handschin, C., and Spiegelman, B.M. (2006). Peroxisome proliferator-activated receptor gamma coactivator 1 coactivators, energy homeostasis, and metabolism. Endocr. Rev. *27*, 728–735. https://doi.org/10.1210/er.2006-0037.

Hell, K., Neupert, W., and Stuart, R.A. (2001). Oxa1p acts as a general membrane insertion machinery for proteins encoded by mitochondrial DNA. EMBO J. *20*, 1281–1288. https://doi.org/10.1093/emboj/20.6.1281.

Hildenbeutel, M., Hegg, E.L., Stephan, K., Gruschke, S., Meunier, B., and Ott, M. (2014). Assembly factors monitor sequential hemylation of cytochrome b to regulate mitochondrial translation. J. Cell Biol. *205*, 511–524. https://doi.org/10.1083/jcb.201401009.

Keil, M., Bareth, B., Woellhaf, M.W., Peleh, V., Prestele, M., Rehling, P., and Herrmann, J.M. (2012). Oxa1-Ribosome complexes coordinate the assembly of cytochrome c oxidase in mitochondria. J. Biol. Chem. *287*, 34484–34493. https://doi.org/10.1074/jbc.m112.382630.

Kulak, N.A., Pichler, G., Paron, I., Nagaraj, N., and Mann, M. (2014). Minimal, encapsulated proteomic-sample processing applied to copy-number estimation in eukaryotic cells. Nat. Methods *11*, 319–324. https://doi.org/10.1038/nmeth.2834.

Latorre-Muro, P., O'Malley, K.E., Bennett, C.F., Perry, E.A., Balsa, E., Tavares, C.D.J., Jedrychowski, M., Gygi, S.P., and Puigserver, P. (2021). A cold-stress-inducible PERK/OGT axis controls TOM70-assisted mitochondrial protein import and cristae formation. Cell Metab. *33*, 598–614.e7. https://doi.org/10.1016/j.cmet.2021.01.013.

Lobo-Jarne, T., Nývltová, E., Pérez-Pérez, R., Timón-Gómez, A., Molinié, T., Choi, A., Mourier, A., Fontanesi, F., Ugalde, C., and Barrientos, A. (2018). Human COX7A2L regulates complex III biogenesis and promotes supercomplex organization remodeling without affecting mitochondrial bioenergetics. Cell Rep. *25*, 1786–1799.e4. https://doi.org/10.1016/j.celrep.2018.10.058.

Lonlay, P. de, Valnot, I., Barrientos, A., Gorbatyuk, M., Tzagoloff, A., Taanman, J.-W., Benayoun, E., Chrétien, D., Kadhom, N., Lombès, A., et al. (2001). A mutant mitochondrial respiratory chain assembly protein causes complex III deficiency in patients with tubulopathy, encephalopathy and liver failure. Nat. Genet. *29*, 57–60. https://doi.org/10.1038/ng706.

Lyons, A., Coleman, M., Riis, S., Favre, C., O'Flanagan, C.H., Zhdanov, A.V., Papkovsky, D.B., Hursting, S.D., and O'Connor, R. (2017). Insulin-like growth factor 1 signaling is essential for mitochondrial biogenesis and mitophagy in cancer cells. J. Biol. Chem. *292*, 16983–16998. https://doi.org/10.1074/jbc.m117.792838.

Martínez-Reyes, I., Cardona, L.R., Kong, H., Vasan, K., McElroy, G.S., Werner, M., Kihshen, H., Reczek, C.R., Weinberg, S.E., Gao, P., et al. (2020). Mitochondrial ubiquinol oxidation is necessary for tumour growth. Nature *585*, 288–292. https://doi.org/10.1038/s41586-020-2475-6.

Mootha, V.K., Handschin, C., Arlow, D., Xie, X., St Pierre, J., Sihag, S., Yang, W., Altshuler, D., Puigserver, P., Patterson, N., et al. (2004). Errα and Gabpa/b specify PGC-1α-dependent oxidative phosphorylation gene expression that is altered in diabetic muscle. Proc. Natl. Acad. Sci. USA *101*, 6570–6575. https://doi.org/10.1073/pnas.0401401101.

Pakos-Zebrucka, K., Koryga, I., Mnich, K., Ljujic, M., Samali, A., and Gorman, A.M. (2016). The integrated stress response. EMBO Rep. *17*, 1374–1395. https://doi.org/10.15252/embr.201642195.

Perez-Riverol, Y., Csordas, A., Bai, J., Bernal-Llinares, M., Hewapathirana, S., Kundu, D.J., Inuganti, A., Griss, J., Mayer, G., Eisenacher, M., et al. (2019). The PRIDE database and related tools and resources in 2019: improving support for quantification data. Nucleic Acids Res. *47*, D442–D450. https://doi.org/10.1093/nar/gky1106.

Priesnitz, C., and Becker, T. (2018). Pathways to balance mitochondrial translation and protein import. Genes Dev. *32*, 1285–1296. https://doi.org/10.1101/gad.316547.118.

Protasoni, M., Pérez-Pérez, R., Lobo-Jarne, T., Harbour, M.E., Ding, S., Peñas, A., Diaz, F., Moraes, C.T., Fearnley, I.M., Zeviani, M., et al. (2020). Respiratory supercomplexes act as a platform for complex III-mediated maturation of human mitochondrial complexes I and IV. EMBO J. *39*, e102817. https://doi.org/10.15252/embj.2019102817.

Puigserver, P., Wu, Z., Park, C.W., Graves, R., Wright, M., and Spiegelman, B.M. (1998). A cold-inducible coactivator of nuclear receptors linked to adaptive thermogenesis. Cell *92*, 829–839. https://doi.org/10.1016/s0092-8674(00)81410-5.

Richter-Dennerlein, R., Oeljeklaus, S., Lorenzi, I., Ronsör, C., Bareth, B., Schendzielorz, A.B., Wang, C., Warscheid, B., Rehling, P., and Dennerlein, S. (2016). Mitochondrial protein synthesis adapts to influx of nuclear-encoded protein. Cell *167*, 471–483.e10. https://doi.org/10.1016/j.cell.2016.09.003.

Riis, S., Murray, J.B., and O'Connor, R. (2020). IGF-1 signalling regulates mitochondria dynamics and turnover through a conserved GSK-3β–Nrf2–BNIP3 pathway. Cells *9*, 147. https://doi.org/10.3390/cells9010147.

Salvatori, R., Kehrein, K., Singh, A.P., Aftab, W., Möller-Hergt, B.V., Forne, I., Imhof, A., and Ott, M. (2020). Molecular wiring of a mitochondrial translational feedback loop. Mol. Cell *77*, 887–900.e5. https://doi.org/10.1016/j.molcel.2019.11.019.

Scarpulla, R.C. (2002). Nuclear activators and coactivators in mammalian mitochondrial biogenesis. Biochim. Biophys. Acta *1576*, 1–14. https://doi.org/10.1016/s0167-4781(02)00343-3.

Scarpulla, R.C. (2008). Transcriptional paradigms in mammalian mitochondrial biogenesis and function. Physiol. Rev. *88*, 611–638. https://doi.org/10.1152/physrev.00025.2007.

Schneider, C.A., Rasband, W.S., and Eliceiri, K.W. (2012). NIH Image to ImageJ: 25 years of image analysis. Nat. Methods *9*, 671–675. https://doi.org/10.1038/nmeth.2089.

Schreiber, S.N., Emter, R., Hock, M.B., Knutti, D., Cardenas, J., Podvinec, M., Oakeley, E.J., and Kralli, A. (2004). The estrogen-related receptor α (ERRα) functions in PPARγ coactivator 1α (PGC-1α)-induced mitochondrial biogenesis. Proc. Natl. Acad. Sci. USA *101*, 6472–6477. https://doi.org/10.1073/pnas.0308686101.

Shalem, O., Sanjana, N.E., Hartenian, E., Shi, X., Scott, D.A., Mikkelson, T., Heckl, D., Ebert, B.L., Root, D.E., Doench, J.G., et al. (2014). Genome-scale CRISPR-Cas9 knockout screening in human cells. Science *343*, 84–87. https://doi.org/10.1126/science.1247005.

Stephan, K., and Ott, M. (2020). Timing of dimerization of the bc 1 complex during mitochondrial respiratory chain assembly. Biochim. Biophys. Acta Bioenerg. *1861*, 148177. https://doi.org/10.1016/j.bbabio.2020.148177.

Tucker, E.J., Wanschers, B.F.J., Szklarczyk, R., Mountford, H.S., Wijeyeratne, X.W., van den Brand, M.A.M., Leenders, A.M., Rodenburg, R.J., Reljić, B., Compton, A.G., et al. (2013). Mutations in the UQCC1-interacting protein, UQCC2, cause human complex III deficiency associated with perturbed cytochrome b protein expression. PLoS Genet. *9*, e1004034. https://doi.org/10.1371/journal.pgen.1004034.

Tyanova, S., Temu, T., Sinitcyn, P., Carlson, A., Hein, M.Y., Geiger, T., Mann, M., and Cox, J. (2016). The Perseus computational platform for comprehensive analysis of (prote)omics data. Nat. Methods *13*, 731–740. https://doi.org/10.1038/nmeth.3901.

Vasseur, M.L., Friedman, J., Jost, M., Xu, J., Yamada, J., Kampmann, M., Horlbeck, M.A., Salemi, M.R., Phinney, B.S., Weissman, J.S., et al. (2021). Genome-wide CRISPRi screening identifies OCIAD1 as a prohibitin client and regulatory determinant of mitochondrial Complex III assembly in human cells. Elife *10*, e67624. https://doi.org/10.7554/elife.67624.

Vercellino, I., and Sazanov, L.A. (2021). The assembly, regulation and function of the mitochondrial respiratory chain. Nat. Rev. Mol. Cell Biol. *23*, 141–161. https://doi.org/10.1038/s41580-021-00415-0.

Wang, Y., and Hekimi, S. (2016). Understanding ubiquinone. Trends Cell Biol. *26*, 367–378. https://doi.org/10.1016/j.tcb.2015.12.007.

Wanschers, B.F.J., Szklarczyk, R., van den Brand, M.A.M., Jonckheere, A., Suijskens, J., Smeets, R., Rodenburg, R.J., Stephan, K., Helland, I.B., Elkamil, A., et al. (2014). A mutation in the human CBP4 ortholog UQCC3 impairs complex III assembly, activity and cytochrome b stability. Hum. Mol. Genet. *23*, 6356–6365. https://doi.org/10.1093/hmg/ddu357.

Weinberg, S.E., Singer, B.D., Steinert, E.M., Martinez, C.A., Mehta, M.M., Martinez-Reyes, I., Gao, P., Helmin, K.A., Abdala-Valencia, H., Sena, L.A., et al. (2019). Mitochondrial complex III is essential for suppressive function of regulatory T cells. Nature *565*, 495–499. https://doi.org/10.1038/s41586-018-0846-z.

Weraarpachai, W., Antonicka, H., Sasarman, F., Seeger, J., Schrank, B., Kolesar, J.E., Lochmüller, H., Chevrette, M., Kaufman, B.A., Horvath, R., et al. (2009). Mutation in TACO1, encoding a translational activator of COX I, results in cytochrome c oxidase deficiency and late-onset Leigh syndrome. Nat. Genet. *41*, 833–837. https://doi.org/10.1038/ng.390.

Wu, Z., Puigserver, P., Andersson, U., Zhang, C., Adelmant, G., Mootha, V., Troy, A., Cinti, S., Lowell, B., Scarpulla, R.C., et al. (1999). Mechanisms controlling mitochondrial biogenesis and respiration through the thermogenic coactivator PGC-1. Cell *98*, 115–124. https://doi.org/10.1016/s0092-8674(00)80611-x.

Zara, V., Palmisano, I., Conte, L., and Trumpower, B.L. (2004). Further insights into the assembly of the yeast cytochrome bc1 complex based on analysis of single and double deletion mutants lacking supernumerary subunits and cytochrome b. Eur. J. Biochem. *271*, 1209–1218. https://doi.org/10.1111/j.1432-1033.2004.04024.x.

Zhang, S., Reljić, B., Liang, C., Kerouanton, B., Francisco, J.C., Peh, J.H., Mary, C., Jagannathan, N.S., Olexiouk, V., Tang, C., et al. (2020). Mitochondrial peptide BRAWNIN is essential for vertebrate respiratory complex III assembly. Nat. Commun. *11*, 1312. https://doi.org/10.1038/s41467-020-14999-2.

STAR★METHODS

KEY RESOURCES TABLE

REAGENT or RESOURCE	SOURCE	IDENTIFIER
Antibodies		
Rabbit polyclonal anti-ACC	Cell signaling Technology	Cat#3662; RRID: AB_2219400
Rabbit monoclonal anti-AKT(pan) (11E7)	Cell signaling Technology	Cat#4685; RRID: AB_2225340
Rabbit monoclonal anti-ATF4	Cell signaling Technology	Cat#11815; RRID: AB_2616025
Mouse monoclonal anti-ATP5A	Santa Cruz	Cat#SC-136178; RRID: AB_2061764
Rabbit polyclonal anti-BRAWNIN	This paper	RRID: AB_11005682
Mouse monoclonal anti-Citrate Synthase	Santa Cruz	Cat#SC-390693; RRID: AB_2813783
Mouse monoclonal anti-COX4I1	AB Clonal	Cat#A10098; RRID: AB_2757620
Rabbit polyclonal anti-CYC1	AB Clonal	Cat#A10449; RRID: AB_2757996
Rabbit polyclonal anti-DYKDDDDK	ProteinTech	Cat#20543-1-AP; RRID: AB_11232216
Rabbit monoclonal anti-GAPDH	Cell signaling Technology	Cat#2118; RRID: AB_561053
Rabbit polyclonal anti-MRPS30	Abclonal	Cat#A5841; RRID: AB_2766591
Rabbit polyclonal anti-MRPS18B	Proteintech	Cat#16139-1-AP; RRID: AB_2146368
Mouse monoclonal anti-MTCO1	Abcam	Cat#Ab14705; RRID: AB_2084810
Rabbit polyclonal anti-MTCO2	ProteinTech	Cat#55070-1-AP; RRID: AB_10859832
Rabbit polyclonal anti-CYTB	ProteinTech	Cat#55090-1-AP; RRID: AB_2881266
Rabbit monoclonal anti-mTOR	Cell signaling Technology	Cat#2983; RRID: AB_2105622
Mouse monoclonal anti-NDUFA9	Invitrogen	Cat#459100; RRID: AB_2532223
Rabbit Monoclonal anti-OXA1L	ProteinTech	Cat#66128-1-IG; RRID: AB_2881527
Rabbit polyclonal anti-phospho-ACC (Ser79)	Cell signaling Technology	Cat#3661; RRID: AB_330337
Rabbit monoclonal anti-phospho-AKT (Ser389)	Abcam	Cat#Ab81283; RRID: AB_2224551
Rabbit monoclonal anti-phospho-mTOR	Cell signaling Technology	Cat#5536; RRID: AB_10691552
Rabbit polyclonal anti-SDHA	AB Clonal	Cat#A2594; RRID: AB_2764479
Rabbit polyclonal anti-SMIM4	Invitrogen	Cat#PA5-61586; RRID: AB_2647649
Mouse monoclonal anti-SOD2	Santa Cruz	Cat#SC-133134; RRID: AB_2191814
Rabbit polyclonal anti-TIM23	ProteinTech	Cat#11123-1-AP; RRID: AB_615045
Rabbit polyclonal anti-TOMM20	ProteinTech	Cat#11802-1-AP; RRID: AB_2207530
Rabbit polyclonal anti-TOMM70	AB Clonal	Cat#A4349; AB_2765636
Mouse monoclonal anti-TUBULIN	ProteinTech	Cat#66031-1-IG; RRID: AB_11042766
Rabbit polyclonal anti-UQCC1	Sigma-Aldrich	Cat#HPA034875; RRID: AB_10603226
Rabbit polyclonal anti-UQCC2	AB Clonal	Cat#A19955; RRID: AB_2862865
Rabbit polyclonal anti-UQCC3	Sigma-Aldrich	Cat#HPA046851; RRID: AB_2679839
Rabbit polyclonal anti-UQCRC1	AB Clonal	Cat#A3339; RRID: AB_2765058
Rabbit polyclonal anti-UQCRC2	AB Clonal	Cat#A4181; RRID: AB_2765543
Mouse monoclonal anti-UQCRFS1	Abcam	Cat#Ab14746; RRID: AB_301445
Chemicals, peptides, and recombinant proteins		
Sucrose	Sigma-Aldrich	Cat#S3089
Ethylenediaminetetraacetic acid, ACS reagent, 99.4–100.6%, powder	Sigma-Aldrich	Cat#E9884
Trizma® base, anhydrous, free-flowing, Redi-Dri™, ≥99.9%	Sigma-Aldrich	Cat#RDD008
Ethylene glycol-bis(2-aminoethylether)-N,N,N′,N′-tetraacetic acid, ≥97.0%	Sigma-Aldrich	Cat#E4378
n-Dodecyl β-D-maltoside, ≥98% (GC)	Sigma-Aldrich	Cat#D4641
Digitonin	Sigma-Aldrich	Cat#D141

(*Continued on next page*)

Continued

REAGENT or RESOURCE	SOURCE	IDENTIFIER
D-Sorbitol, ≥98%	Sigma-Aldrich	Cat#S1876
ANTI-FLAG® M2 Affinity Gel, purified immunoglobulin, buffered aqueous glycerol solution	Sigma-Aldrich	Cat#A2220
3X FLAG® Peptide, lyophilized powder	Sigma-Aldrich	Cat#F4799
Sodium chloride, ReagentPlus®, ≥99%	Sigma-Aldrich	Cat#S9625
Potassium chloride, powder, BioReagent, suitable for cell culture, suitable for insect cell culture, ≥99.0%	Sigma-Aldrich	Cat#P5405
Lipofectamine 3000	Invitrogen	Cat#L3000015
Hexadimethrine bromide, ≥94% (titration)	Sigma-Aldrich	Cat#H9268
Puromycin	Invivogen	Cat#ant-pr
G418	Invivogen	Cat#ant-gn
Blotting-Grade Blocker	Bio-Rad	Cat#1706404
20X Tris Buffered Saline (TBS) Buffer, Ultra Pure Grade	1st base	Cat#BUF-3030-20X4L
TWEEN® 20, viscous liquid	Sigma-Aldrich	Cat#P1379
NativePAGE™ Running Buffer (20X)	Invitrogen	Cat#BN2001
NativePAGE™ Cathode Buffer Additive (20X)	Invitrogen	Cat#BN2002
NativePAGE™ 5% G-250 Sample Additive	Invitrogen	Cat#BN2004
NativePAGE™ Sample Buffer (4X)	Invitrogen	Cat#BN2003
20X MES SDS Running Buffer	Invitrogen	Cat#B0002
cOmplete™, Mini Protease Inhibitor Cocktail	Roche	Cat#11836153001
cOmplete™, Mini, EDTA-free Protease Inhibitor Cocktail	Roche	Cat#11836170001
Methanol, for analysis EMSURE® ACS,ISO,Reag. Ph Eur	Merck	Cat#1.06009.2511
Acetic acid (glacial) 100%, anhydrous for analysis EMSURE® ACS,ISO,Reag. Ph Eur	Merck	Cat#1.00063.2500
Chloroform, >99.0%(GC)	Kanto Chemical	Cat#07278-00
EXPRE^{35}S^{35}S Protein Labeling Mix, [^{35}S]-, 2mCi (74MBq), 50mM Tricine (pH 7.4), 10mM 2-mercaptoethanol	Perkin Elmer	Cat#NEG072002MC
L-Methionine. reagent grade, ≥98% (HPLC)	Sigma-Aldrich	Cat#M9625
L-Cysteine, 97%	Sigma-Aldrich	Cat#168149
Sodium carbonate, BioUltra, anhydrous, ≥99.5% (calc. on dry substance, T)	Sigma-Aldrich	Cat#71345
Insulin solution human, sterile-filtered, BioXtra, suitable for cell culture	Sigma-Aldrich	Cat#I9278
IGF-I human Animal-component free, recombinant, expressed in E. coli, ≥98% (SDS-PAGE), ≥98% (HPLC), suitable for cell culture	Sigma-Aldrich	Cat#SRP3069
AICAR	MCE	Cat#HY-13417
DMEM/High glucose (4500mg/mL) with L-glutamine; without sodium pyruvate	HyClone	Cat#SH30022.01
DMEM/Low glucose (1000mg/mL) with L-glutamine, sodium pyruvate	HyClone	Cat#SH30021.01
DMEM, high glucose, no glutamine, no methionine, no cystine	Gibco	Cat#21013024
Sodium pyruvate solution, 100 mM, sterile-filtered, BioReagent, suitable for cell culture	Sigma-Aldrich	Cat#S8636
Penicillin-Streptomycin (10,000 U/mL)	Gibco	Cat#15140-122
Fetal Bovine Serum, South American Origin, Heat Inactivated	HyClone	Cat#SV30160.03
Fetal Bovine Serum, dialyzed, US origin	Gibco	Cat#26400-044
Triton™ X-100, laboratory grade	Sigma-Aldrich	Cat#X100

(*Continued on next page*)

Continued

REAGENT or RESOURCE	SOURCE	IDENTIFIER
Bovine Serum Albumin, heat shock fraction, protease free, fatty acid free, essentially globulin free, pH 7, ≥98%	Sigma-Aldrich	Cat#A7030
Sodium deoxycholate, ≥97% (titration)	Sigma-Aldrich	Cat#D6750
Sodium dodecyl sulfate, BioReagent, suitable for electrophoresis, for molecular biology, ≥98.5% (GC)	Sigma-Aldrich	Cat#L3771
Glycerol, ACS reagent, ≥99.5%	Sigma-Aldrich	Cat#G7893
HEPES, ≥99.5% (titration)	Sigma-Aldrich	Cat#H3375
Magnesium chloride, anhydrous, ≥98%	Sigma-Aldrich	Cat#M8266
Ambion™ RNase I, cloned, 100 U/μL	Invitrogen	Cat#AM2294
SUPERase●In™ RNase Inhibitor (20 U/μL)	Invitrogen	Cat#AM2694
L-Glutamine (200 mM)	Gibco	Cat#25030081
D-(+)-Glucose solution, 100 g/L in H2O, sterile-filtered, BioXtra, suitable for cell culture	Sigma-Aldrich	Cat#G8644
D-(+)-Galactose, powder, anhydrous, BioReagent, suitable for cell culture, suitable for insect cell culture	Sigma-Aldrich	Cat#G5388
Oligomycin A, ≥99% (HPLC)	Sigma-Aldrich	Cat#75351
Carbonyl cyanide 4-(trifluoromethoxy)phenylhydrazone ≥98% (TLC), powder	Sigma-Aldrich	Cat#C2920
Rotenone, ≥95%	Sigma-Aldrich	Cat#R8875
Antimycin A from Streptomyces sp.	Sigma-Aldrich	Cat#A8674
5,5′-Dithiobis(2-nitrobenzoic acid), ≥98%, BioReagent, suitable for determination of sulfhydryl groups	Sigma-Aldrich	Cat#D8130
Acetyl coenzyme A, trilithium salt, trihydrate	MP Biomedicals	Cat#100490
Oxaloacetic acid, ≥97% (HPLC)	Sigma-Aldrich	Cat#O4126
Trypsin-EDTA (0.25%), phenol red	Gibco	Cat#25200-056
DPBS without calcium, magnesium	HyClone	Cat#SH30028.02
Sodium hydroxide, reagent grade, 97%, powder	Sigma-Aldrich	Cat#655104
Agarose	1st base	Cat#BIO-1000
2-Chloroacetamide, ≥98%	Sigma-Aldrich	Cat#C0267
Bond-Breaker™ TCEP Solution, Neutral pH	Thermo Fisher Scientific	Cat#77720
Pierce™ Trypsin Protease, MS Grade	Thermo Fisher Scientific	Cat#90057
Trifluoroacetic acid, eluent additive for LC-MS, LiChropur, ≥99.0% (GC)	Sigma-Aldrich	Cat#80457
Acetonitrile, anhydrous, 99.8%	Sigma-Aldrich	Cat#271004
Ammonium hydroxide solution, puriss., 30–33% NH3 in H2O	Sigma-Aldrich	Cat#05002
Pierce™ Formic Acid, LC-MS Grade	Thermo Fisher Scientific	Cat#TS-28905
Acetone, ACS reagent, ≥99.5%	Sigma-Aldrich	Cat#179124
Urea AR	Chem-Supply	Cat#UA001
Ammonium bicarbonate, BioUltra, ≥99.5% (T)	Sigma-Aldrich	Cat#09830
SYBRSafe	Sigma-Aldrich	Cat#S33102
TRIzol LS Reagent	ambion	Cat#10296028
Critical commercial assays		
Pierce BCA Protein Quantification Kit	Thermo	Cat#23225
iScript Reverse Transcription Supermix for RT-qPCR	Bio-Rad	Cat#1708841
iTaq Universal SYBR Green Supermix	Bio-Rad	Cat#1725124
Deposited data		
Mass spectrometry proteomics data	This paper	ProteomeXchange Consortium: PXD030258

(*Continued on next page*)

Continued

REAGENT or RESOURCE	SOURCE	IDENTIFIER
Experimental models: Cell lines		
Human HEK293T	ATCC	Cat#CRL-3216
Mouse C2C12	ATCC	Cat#CRL-1772
Experimental models: Organisms/strains		
Mouse: WT (C57BL/6J)	The Jackson Laboratory	Cat#000664
Mouse: BR$^{-/-}$ (C57BL/6J)	This paper	NA
Oligonucleotides		
For genotyping primers, gRNAs, and qPCR primers, see Table S3	N/A	N/A
Recombinant DNA		
lentiCRISPRv2 puro	Gift from Shang Li Lab	NA
psAAV-CMV-mBrawnin-FLAG	This paper	NA
psAAV-CMV-mSmim4-FLAG	This paper	NA
psAAV-CMV-GFP	This paper	NA
pCDH-CMV-mSmim4-FLAG	This paper	NA
pCDH-CMV-mBrawnin-FLAG	This paper	NA
pCDH-CMV-mC16orf91-FLAG	This paper	NA
pCDH-CMV-mUqcc1-FLAG	This paper	NA
pCDH-CMV-mUqcc3-FLAG	This paper	NA
pCDH-CMV-mUqcrq-FLAG	This paper	NA
Software and algorithms		
ImageJ	Schneider et al., 2012	https://imagej.nih.gov/ij/
Image Lab Software for PC Version 6.1	Bio-Rad	SOFT-LIT-170-9690-ILSPC-V-6-1
MaxQuant platform	MaxQuant	(version 1.6.17.0)
Perseus framework	Perseus	(version 1.6.10.43)
PyMOL 2	PyMOL	https://pymol.org/2/

RESOURCE AVAILABILITY

Lead contact

Further information and requests for resources and reagents should be directed to and will be fulfilled by the lead contact, Lena Ho (lena@ho-lab.org).

Materials availability

Unique reagents generated in this study will be made available upon reasonable request to the lead contact with a completed Materials Transfer Agreement.

Data and code availability

- The mass spectrometry proteomics data have been deposited to the ProteomeXchange Consortium via the PRIDE partner repository with the dataset identifier PXD030258 (Perez-Riverol et al., 2019).
- No new code has been generated in this study.
- Any additional information required to reanalyze the data reported in this paper is available from the lead contact upon request.

EXPERIMENTAL MODEL AND SUBJECT DETAILS

Animals

C57BL/6J mice were obtained from Jackson laboratory and housed at 21–24°C with relative humidity maintained at 40–60%. Water and chow diet were provided ad libitum. All the animal protocols have approved by the Duke-NUS, SingHealth Institutional Animal Care and Use Committee. 9 weeks old female mice were used for the heart mitochondrial proteomics analysis. 20 weeks old male mice were used in the treadmill exercise experiment. Gender paired male and female P6 pups were injected with AAV for expressing protein of interest and sacrificed 6 weeks after the infection.

Cell lines

Cells were cultured at 37°C with 5% CO_2 unless stated otherwise. C2C12 (CRL-1772) myoblast was maintained at sub-confluent densities in DMEM high glucose (4500 mg/mL) medium supplemented with 10% FBS, 1 mM pyruvate and 100 U/mL penicillin-streptomycin.HEK293T (CRL-3216) was maintained in the same medium as C2C12 myoblast. Both cell lines were obtained from ATCC and no further authentication was performed.

METHOD DETAILS

Cell culture

Cell lines were maintained at sub-confluency. Cells were washed with PBS before being digested with 0.25% Trypsin-EDTA for 3 min at 37°C. Trypsin was neutralized with equal volumes of complete DMEM media. Cell pellet was collected through centrifugation for 3 min at 300 ×*g*. Desired number of cells were plated back with complete DMEM media or otherwise indicated.

Experiments involving drug treatment were performed with 250 nM insulin, or 500 μM AICAR, or 500 μg/mL IGF-1, or 100 mM oligomycin. Glucose deprivation experiment was conducted using DMEM media without glucose supplemented with 4 mM glutamine, 10% FBS, 1mM sodium pyruvate and 100 U/mL of Pen/Strep. Galactose treatment experiments was conducted using Low Glucose (1000 mg/mL) Media supplemented with 4 mM glutamine, 10 mM galactose, 10% dialyzed FBS, 1 mM sodium pyruvate and 100 U/mL of Pen/Strep. For cold challenge, cells were maintained at 28°C with 5% CO_2. Samples were collected at respective time points.

Plasmid construction

Protein coding sequences of mouse BRAWNIN, SMIM4, C16ORF91, UQCC1, UQCC3, and UQCRQ were amplified from cDNA of C2C12 cell, tagged with FLAG by PCR and inserted into the XhoI-NotI sites of the pCDH-CMV vector by In-Fusion cloning. Similarly, protein coding sequences of GFP, mouse BRAWNIN and SMIM4 were inserted into the AgeI-NotI sites of the psAAV-CMV vector.

BR KO mouse generation and genotyping

BR KO mouse lines were generated by pronuclear injection of Cas9 proteins and gRNAs (sequence in key resource table) into C57BL/6J mice. Injected animals were backcrossed to wild type C57BL/6J mice for 8 generations. Homozygous KO and wild type control animals were obtained by intercrossing of heterozygous KOs. To determine the genotype of crossed animals, mouse tail clips were collected and digested in HOTSHOT lysis buffer (25 mM NaOH, 0.2 mM EDTA) at 95°C for 2 h followed by neutralization with equal volume of 80 mM Tris-HCl pH 3.0. The genomic locus was amplified by PCR using KOD FX neo (Toyobo) with the list primers (See key resource table) in a Bio-Rad C1000 Touch Thermal Cycler with annealing temperature set to 62°C. The WT and CRISPR edited strands produced DNA products of 393 bp and 300bp, respectively. PCR products were stained with SYBR Safe (1:10,000) and resolved in a 2% agarose gel.

Mouse treadmill exercise

WT and BR KO male mice of the same litter at 20 weeks were selected to perform treadmill exercise. Mice were habituated to a single-line enclosed metabolic treadmill equipped with a shock grid (Columbus Instruments) for 3 days prior to experiments. The exhaustive exercise test began with 10-min 0 m/min acclimation period followed by a speed of 6m/min for 5 min, followed by increasing speed 3 m/min every 5 min. Once 20 m/min was reached, speed increased by 2 m/min every 2 min until exhaustion, defined as remaining on the shock grid for 10 seconds without engaging the treadmill. Oxygen consumption and carbon dioxide production were continually measured by indirect calorimetry and used to determine RER.

Mitochondria isolation

Mitochondria were isolated from mouse tissues and cultured cells as described by Fernández-Vizarra, et al. and Acín-Pérez et al., respectively (Acín-Pérez et al., 2008; Fernández-Vizarra et al., 2010).

Briefly, mice were euthanized by CO_2 and desired tissues were immediately dissected after perfusions with PBS. Heart and skeletal muscles were minced carefully with a scissor and incubated 10 volumes of heart mitochondria isolation buffer (75 mM sucrose, 225 mM sorbitol, 1mM EGTA, 0.1% fatty acid free BSA, 10 mM Tris-HCl, pH7.4) or skeletal muscle mitochondria isolation buffer (67 mM sucrose, 50 mM KCl, 10 mM EDTA, 0.1% fatty acid free BSA, 50 mM Tris-HCl, pH7.4) supplemented with 1x cOmplete protease inhibitors and 1mM PMSF. Minced tissues were dounced in Potter-Elvehjem tissue grinders with PTFE pestles driven by a motorized drill for 10 to15 strokes. Efficiency of tissue homogenization was inspected by white field microscopy. Homogenates were transferred to tubes and spun at 600 ×*g* for 10 min at 4°C. The supernatant was collected and spun at 7000 ×*g* for 15 min at 4°C. The mitochondria pellet was gently resuspended in Buffer C (320 mM sucrose, 1mM EDTA, 10mM Tris-HCl, pH7.4). Mitochondrial protein content was measured by BCA assay. Desired quantity of mitochondria was aliquoted and pelleted at 7000 ×*g* for 15 min at 4°C. Mitochondria pellets were used directly or stored at −80°C for future biochemical analysis.

For isolating mitochondria from cultured cells, cell pellets were harvested, washed in PBS and then resuspended in Buffer A (83 mM sucrose, 10 mM HEPES pH7.4) supplemented with 1x cOmplete protease inhibitors and 1mM PMSF, and incubated for 10 min on ice. Cells were then dounced in Potter-Elvehjem tissue grinders as described above. Homogenates were spun at

1,000 ×*g* for 10 min at 4°C. The supernatant was transferred to a new tube and remaining pellets were resuspended again in Buffer B (250 mM sucrose, 10 mM HEPES pH7.4) supplemented with 1x cOmplete protease inhibitors and 1mM PMSF. The extraction was repeated, and homogenates were spun at 1,000 ×*g* for 10 min at 4°C. The supernatant of both extractions was combined and spun at 12,000 ×*g* for 15 min at 4°C. The mitochondria pellet was resuspended in Buffer C supplemented with 1x cOmplete protease inhibitors and 1mM PMSF with protein content quantified using a Pierce BCA kit.

Mouse heart mitochondrial proteome analysis

Mouse heart mitochondria were isolated as described above. Frozen mitochondria pellets were solubilized in 1% (w/v) sodium deoxycholate (SDC), 100 mM Tris pH 8.1, 40 mM chloroacetamide, 10 mM tris(2-carboxyethyl)phosphine hydrochloride (TCEP). Samples were briefly vortexed then boiled for 5 min at 99°C with 1500 rpm of shaking, then sonicated for 15 mins in a water bath, before adding a 1:50 ratio (μg: μg) of trypsin and incubated at 37°C overnight. Samples were then centrifuged at max speed for 10 minutes at room temperature before supernatant was transferred to 3x14G SDB-RPS plug stagetips. Stagetips were washed twice with ethyl acetate containing 1% trifluoroacetic acid (TFA) and once with 0.2% TFA. Peptides were eluted in 80% acetonitrile (ACN), 1% ammonium hydroxide. All centrifugation steps were performed at 3000 ×*g* at room temperature. Samples were acidified to 1% TFA and dried using a CentriVap concentrator (Labconco) before being reconstituted in 0.1% TFA, 2% ACN and analysed via LC-MS/MS, carried out on an Orbitrap QExactive Plus (Thermo Scientific) coupled with an Ultimate 3000 RSLC nanoHPLC (Dionex Ultimate 3000). The LC system was equipped with an Acclaim Pepmap nano-trap column (Dinoex-C18, 100 Å, 75 μm × 2 cm) and an Acclaim Pepmap RSLC analytical column (Dinoex-C18, 100 Å, 75 μm × 50 cm). The tryptic peptides were injected to the enrichment column at an isocratic flow of 5 μL/min of 2% ACN (v/v) containing 0.1% formic acid (v/v) for 5 min applied before the enrichment column was switched in-line with the analytical column. The eluents were 5% DMSO in 0.1% formic acid (v/v) (solvent A) and 5% DMSO in 100% ACN (v/v) and 0.1% formic acid (v/v) (solvent B). The flow gradient was (i) 0–6 min at 3% B, (ii) 6–95 min, 3–22% B (iii) 95–105 min 22–40% B (iv) 105–110min, 40–80% B (v) 110–115min, 80–80% B (vi) 115–117min, 80–3% and equilibrated at 2% B for 10 minutes before the next sample injection.

The QExactive plus mass spectrometer was operated in the data-dependent mode, whereby full MS1 spectra were acquired in positive mode, 70 000 resolution, AGC target of $3e^6$ and maximum IT time of 50ms. Fifteen of the most intense peptide ions with charge states ≥ 2 and intensity threshold of $4e^4$ were isolated for MSMS. The isolation window was set at 1.2m/z and precursors fragmented using normalized collision energy of 30, 17 500 resolution, AGC target of $5e^4$ and maximum IT time of 50ms. Dynamic exclusion was set to be 30sec.

Raw files were analysed using MaxQuant platform (Cox and Mann, 2008)(version 1.6.2.10) and searched against UniProt mouse database (25198 entries, September 2018) using default LFQ search parameters with the following modifications: LFQ min. ratio count and label min. ratio count = 1. For this search Trypsin/P cleavage specificity (cleaves after lysine or arginine, even when proline is present) was used with a maximum of 2 missed cleavages. Oxidation of methionine and N-terminal acetylation were specified as variable modifications. Carbamidomethylation of cysteine was set as a fixed modification. A search tolerance of 4.5 ppm was used for MS1 and 20 ppm for MS2 matching. False discovery rates (FDR) were determined through the target-decoy approach set to 1% for both peptides and proteins. Data analysis was conducted using the Perseus framework (Tyanova et al., 2016)(version 1.6.2.2). Briefly, LFQ intensity values were grouped into wild-type and BRAWNIN KO groups consisting of two replicates each. Identifications filtered to include 100% valid values across all samples. Annotations for proteins present in the Mitocarta2.0 dataset (Calvo et al., 2015) were added through matching by gene name and rows filtered to include only mitochondrial entries. Intensities were normalised through subtracting the median. A two-sample t-test was conducted with results displayed as a volcano plot.

SDS-PAGE and immunoblotting

Cell pellets, purified mitochondria, and mouse tissues were lysed in RIPA buffer (10mM Tris-HCl, pH8.0, 1% Triton X-100, 0.5% sodium deoxycholate, 0.1% SDS, 140mM NaCl) supplemented) with 1x cOmplete protease inhibitors and 1mM PMSF. For tough mouse tissues like skeletal and heart, samples were lysed on a MagNA Lyser (Roche) by two 30 s cycles at 5000 rpm. Protein concentrations were determined by a BCA assay (Thermo). After protein concentration normalization, lysates were mixed with 4× protein loading buffer (0.2M Tris-HCl, pH6.5, 50 mM DTT, 8% SDS, 4.3M glycerol) and incubated at 95°C for 5 min in a thermomixer. Proteins were then resolved on 4–12% Bis-Tris precast gels using MES running buffer and transferred to PVDF membranes (Bio-Rad) using a Trans-Blot Turbo system (Bio-Rad). Membranes were blocked in milk TBST (5% skim milk powder dissolved in TBS with 0.1% Tween 20) for 1 h at room temperature and incubated with diluted primary antibodies in milk TBST at 4°C for overnight. Membranes were then extensively washed and incubated with appropriate HRP conjugated secondary antibodies at room temperature for 1 h in milk TBST and extensively washed again. ECLs were prepared following the user manual and evenly distributed to membranes. Chemiluminescence was recorded by a Chemidoc Touch imager. Quantifications were performed using Image Lab.

Native PAGE

Mitochondrial proteins were solubilized in 1xNative PAGE Sample Buffer supplemented with 8 g of digitonin per g of mitochondrial protein and 1x Complete protease inhibitor for 20 min on ice. Lysate was cleared by spin at 20,000 ×*g* for 10 min at 4°C and then supplemented with 0.5% G250 sample additive. Mixed solutions were loaded onto 3–12% Native PAGE Bis-Tris gels. Electrophoresis was performed at 150V for 30 min in the presence of dark blue cathode running buffer and then at 250V for 1 h with light blue

cathode running buffer with ice bath. NativePAGE gels were then imaged with the Coomassie Blue mode on a Bio-Rad Chemidoc Touch imager before transferred to PVDF membranes (Bio-Rad) using a Trans-Blot Semi-Dry system (Bio-Rad). Membranes were then fixed with 8% acetic acid for 15 min before washing in water for 5 min. Membranes were destained in methanol until bands were barely visible and then blocked in 5% milk TBST for 1h at RT. Membranes were then processed as standard western blots.

Gene editing by CRISPR

gRNA cloning protocol is adapted from (Shalem et al., 2014). Oligos of gRNA sequences with appropriate links (CACCG added to forward oligo 5' end; AAAC———C added to reverse oligo 5' and -3′ ends) were obtained from IDT. gRNAs were then cloned into Lenti-CrisprV2-Puro plasmid using BsmBI digestion and T4 ligation as described in Shalem et al. gRNA sequences used for Crispr-Cas9 editing were included in Key Resource Table. Sequence of constructs was validated by Sanger sequencing using a U6 promoter primer.

Virus production and transduction

4.4 million HEK293T cells were seeded in 10 cm dishes the day before transfection. On the day, 3 μg of respective lentiviral plasmids were transfected using Lipofectamine 3000 with other 3rd generation lentivirus production plasmids, namely pMDL, pREV, and pVSVG. The transfectants were left in culture for 6 hours before being exchanged with complete DMEM media. Crude virus was collected at 36 h and 60 h after the transfection. Vivaspin 100,000 MWCO columns (Sartorius) were used to purify and concentrate crude viruses.

25,000 C2C12 cells were seeded in 12 well plates the day before transduction. Appropriate amounts of virus were mixed with 8 μg/mL of hexadimethrine bromide (polybrene) before being added to respective wells for transduction. Cells were subcultured 3 days after transduction and selected with puromycin (1 μg/mL) or G418 (500 μg/mL).

AAV production and infection

ORFs encoding the respective protein of interest with C-terminal FLAG-tag were cloned into psAAV-CMV construct. All constructs were delivered by AAV9 and the viruses were produced by Vector Core @ GIS (A*STAR, Singapore). To deliver the AAVs to target the cardiac muscle, we performed intrathoracic injection of P6 pups using a dose of 1 x 10^10 vg per mouse. The pups were cryoanesthetized on ice prior to injection and allowed to recover under a heat lamp before being returned to the dam. Tissues were collected 6 weeks after neonatal AAV delivery.

Protein co-immunoprecipitation and mass spectrometry

Mitochondria isolated from cell lines and tissues were solubilized in IP buffer (100 mM NaCl, 10% glycerol, 1 mM EDTA, 25 mM Tris-HCl, pH7.4) supplemented with 1% Digitonin (w/v) or 1% Triton-X and 1% SDS. Ratio between digitonin and mitochondria protein was kept at 8g/g. Lysate was nutated for 1 h at 4°C before being spun at 20, 000 ×*g* for 15 min. 2% of the supernatant were kept as input and were supplemented with 1× protein loading dye. For endogenous IP, Protein A/G agarose were pre-incubated and nutated with respective antibody for 1h at 4°C. Remaining supernatant was incubated with anti-FLAG M2 agarose affinity gel or Protein A/G agarose nutating at 4°C for 3 hours or overnight respectively. Beads and bound proteins were spun down at 2,000 ×*g* for 2 min and washed at least 4 times with IP wash buffer (100 mM NaCl, 1 mM EDTA, 25 mM Tris-HCl, pH7.4) supplemented with 0.1% digitonin (w/v) or 0.1% Triton-X and 0.1% SDS. For Flag-IP, beads were then nutating at 4°C for at 30 min together with 35 μL of 100 ng/mL 3× FLAG peptide to elute the bound proteins. For endogenous IP, beads were then boiled at 95°C for 15mins in 35μL of 50mM Tris-HCl with 1% SDS. Eluate was then passed through Pierce Microspin Columns (Thermo) to remove remaining beads. The cleared eluates were then stored at −80°C or used directly for heme assays.

For analysis by mass spectrometry, eluates were precipitated with 5× volumes of ice-cold acetone for 2 h at −20°C. Samples were centrifuged at max speed at 4°C for 10 min and the precipitated protein pellet was washed with additional ice-cold acetone followed by centrifugation. The pellet was solubilised in 8 M urea, 50 mM ammonium bicarbonate (ABC) followed by 15 min of sonication in a sonicator water bath. To reduce and alkylate proteins, TCEP and chloroacetamide were added to a final concentration of 10 mM and 50 mM respectively and incubated at 37°C for 30 min while shaking. Samples were diluted with 50 mM ABC to 2 M urea prior to digestion with 1 μg of trypsin at 37°C overnight. Peptides were acidified to 1% TFA and desalted using stagetips (Kulak et al., 2014) containing 2 × 14G plugs of 3M™ Empore™ SDB-XC Extraction Disks (Sigma-Aldrich) which were pre-activated with 100% ACN and equilibrated with 0.1% TFA, 2% ACN prior to sample loading. Stagetips were washed with 0.1% TFA, 2% ACN and peptides were eluted in 80% ACN, 0.1% TFA. All centrifugation steps were performed at 1800 g at room temperature. Elutions were dried using CentriVap concentrator (Labconco) and samples were reconstituted in 0.1% TFA, 2% ACN and analysed via LC-MS/MS, carried out on an Orbitrap Exploris 480 (Thermo Scientific) coupled with an Ultimate 3000 RSLC nanoHPLC (Dionex Ultimate 3000). The LC system was equipped with an Acclaim Pepmap nano-trap column (Dinoex-C18, 100 Å, 75 μm × 2 cm) and an Acclaim Pepmap RSLC analytical column (Dinoex-C18, 100 Å, 75 μm × 50 cm). The tryptic peptides were injected to the enrichment column at an isocratic flow of 5 μL/min of 2% ACN (v/v) containing 0.1% formic acid (v/v) for 5 min applied before the enrichment column was switched in-line with the analytical column. The eluents were 5% DMSO in solvent A and 5% DMSO in solvent B. The flow gradient was (i) 0–6 min at 3% B, (ii) 6–35 min, 3–22% B (iii) 35–45min 22–40% B (iv) 45–50min, 40–80% B (v) 50–55min, 80–80% B (vi) 55–56min, 80–3% and equilibrated at 2% B for 10 minutes before the next sample injection.

The mass spectrometer was operated in the data-dependent acquisition mode, whereby full MS1 spectra were acquired in a positive mode at 120000 resolution. The 'top speed' acquisition mode with 3 s cycle time on the most intense precursor ion was used, whereby ions with charge states of 2 to 7 were selected. MS/MS analyses were performed by 1.6 *m/z* isolation with the quadrupole, fragmented by HCD with collision energy of 30%. MS2 resolution was at 15000. Dynamic exclusion was activated for 30 s. AGC target was set to standard with auto maximum injection mode. Dynamic exclusion was activated for 30s.

Raw files were analysed using MaxQuant platform (Cox and Mann, 2008) (version 1.6.17.0) and searched against UniProt mouse database (86624 entries, March 2021) using default LFQ search parameters with the following modifications: LFQ min. ratio count and label min. ratio count = 1. For this search Trypsin/P cleavage specificity (cleaves after lysine or arginine, even when proline is present) was used with a maximum of 2 missed cleavages. Oxidation of methionine and N-terminal acetylation were specified as variable modifications. Carbamidomethylation of cysteine was set as a fixed modification. A search tolerance of 4.5 ppm was used for MS1 and 20 ppm for MS2 matching. False discovery rates (FDR) were determined through the target-decoy approach set to 1% for both peptides and proteins. Data analysis was performed using Perseus framework (Tyanova et al., 2016) (version 1.6.10.43). Briefly, LFQ intensities imported from the proteinGroups.txt output were Log_2 transformed. Only proteins quantified in at least two of the three IP samples (with no restrictions on control identifications) were included and the missing control values imputed at the limit of detection based on normal distribution. Experimental groups were assigned to each set of triplicates and a two-sample t-test was conducted with either results displayed as a volcano plot or the fold change plotted against the mean of the FLAG-tagged group Log_2 LFQ intensity.

Polysome profiling and ribosome association

Isolated mitochondria from HEK293T cells were permeabilized with 6 g/g digitonin in ice-cold polysome lysis buffer (20 mM HEPES pH7.4, 100 mM KCl, 20 mM $MgCl_2$, 2 mM DTT, 500 U/mL RNasin and 1x cOmplete Protease Inhibitor, EDTA-free). Clarified mitochondrial lysates were layered over 5 to 30% linear sucrose gradients in sucrose buffer (20 mM HEPES pH7.4, 100 mM KCl, 20 mM $MgCl_2$, 2 mM DTT, 20 U/mL SUPERase●In). Gradients were spun at 36,000 rpm for 2.5 h, using a SW41Ti rotor in a Beckman Coulter Optima L-100XP ultracentrifuge. After ultracentrifugation, gradients were fractionated with a Biocomp Gradient Station fractionator, and separated into 15 fractions. Absorbance at 254 nm was measured using Triax^{TM} Flow Cell (Biocomp) to visualize the separation of ribosomes. Proteins from each fraction were extracted using methanol/chloroform, and loaded onto a 4–12% gel for SDS-PAGE.

Sucrose gradient fractionation

Isolated mitochondria from mouse heart were solubilized with 8g of digitonin per g of protein in 1x NativePAGE sample buffer with 1x Complete protease inhibitor. Lysates were spun down at 20,000 ×*g* for 10 min before layered over a 5 to 60% linear sucrose gradient in sucrose buffer D (25 mM Tris-HCl pH7.4, 60 mM KCl) with 0.1% digitonin (w/v). Gradients were spun at 38,400 rpm for 18 h using a SW41Ti rotor in a Beckman Coulter Optima L-100XP ultracentrifuge. After centrifugation, gradients were fractionated manually at 700 μL per fraction to 17 fractions. Proteins from each fraction were extracted using methanol/chloroform, and loaded onto a 4–12% Bis-Tris gel for SDS-PAGE.

Mitochondria membrane fractionation assay

Freshly isolated mitochondria were treated with different concentrations (0–0.25%) of digitonin in Buffer C for 1 h at 4°C. Samples were then spun down at 20,000 ×*g* for 10 min to separate the supernatant and pellet. The supernatant was transferred to a fresh tube while the pellet was dissolved in equal volume of RIPA buffer. Samples were then supplemented with 1× protein loading dye and boiled at 95°C for 5 min before being analyzed by SDS-PAGE and immunoblotting.

Protease sensitivity assay

Freshly isolated mitochondria were subjected to different concentrations (0–0.3%) of digitonin or 1% Triton X-100 for 10 min on ice. 100 μg/mL of Proteinase K was added to designated tubes and incubated for 30 min on ice. 8 mM of freshly made PMSF was added to stop the digestion. Samples were then supplemented with 1x protein loading dye and boiled at 95°C for 5 min before being analyzed by SDS-PAGE and immunoblotting.

Membrane association assay

Sodium carbonate or KCl were used for the salt extraction assay. Appropriate amounts of salt solutions were added to isolated mitochondria from C2C12 of wanted genotypes. The homogenized solution was kept on ice for 1 hour before being spun down at top speed for 30mins. Pellets were solubilized in RIPA buffer with 1× cOmplete protease inhibitor. 1× protein loading dye was further supplemented to both pellet and supernatant tubes before loading onto 4–12% Bis-Tris gels for SDS-PAGE.

Mitochondrial translation metabolic labeling

Protocols of mitochondrial translation metabolic labeling were adapted from (Chomyn, 1996). To assess the translation efficiency of mitochondrial genome, 250,000 C2C12 cells were seeded in 6-well plates the day before the metabolic labeling assay. On the day, cells were washed with wash media (DMEM High Glucose without Methionine and Cysteine supplemented with 1 mM sodium

pyruvate and 2 mM glutamine) twice with a 10 min incubation at 37°C with 5% CO_2. Labeling media (DMEM High Glucose without Methionine and Cysteine supplemented with 10% dialyzed FBS, 1 mM sodium pyruvate and 2 mM glutamine) were then added together with 100 μg/mL of emetine to inhibit cytosolic protein translation. 22μCi/mL of S^{35}-methionine and cysteine were added to cells to start the pulse labeling. At 10, 30, 60 min, the labeling was stopped by adding 1mM cold methionine and cysteine, and cells were washed with PBS twice before trypsinization. Cell pellets were washed with ice-cold PBS again and lysed with RIPA buffer supplemented with 1× cOmplete protease inhibitor. Cleared lysates were then supplemented with 1× protein loading dye and incubated at 37°C for 5 min. 5% of lysates was quantified with scintillation using Tri-Carb system (Perkin Elmer) for normalization. Samples were then resolved by 16% Bis-Acrylamide gels for 2 h at 150V. Gels were then dried on a vacuum drier (Thermo) for 2.5 h at 70°C on filter papers. Dried gels were exposed with a cleared phosphor-imaging screen (Cytiva) for desired time before being scanned with a typhoon scanner (GE Health).

To assess the stability of mitochondrial genome-encoded proteins, 200K C2C12 cells (6 well-plate) of wanted genotype were seeded 2 days before the pulse-chase assay. 50 μg/mL of chloramphenicol was added to samples at least 16 h before the assay. Procedures were performed as the pulse assay except that 100 μg/mL of cycloheximide was used to inhibit cytosolic translation and after the pulse, cells were washed with non-labelled complete DMEM media thrice before incubating with complete DMEM for indicated time period (0 h, 4 h, 6h). Samples were collected and extracted by RIPA buffer.

To perform protein co-IP after metabolic labeling, 1.2 million C2C12 cells were seeded in 10 cm dish 2 days before the IP assay. 50 μg/mL of chloramphenicol was added to samples at least 16 h before the assay. Procedures were performed as the pulse assay except that cells were labeling for 2 h and cell pellets were lysed with 800 μL of IP buffer (100mM NaCl, 10% glycerol, 1mM EDTA, 25 mM Tris-HCl, pH7.4) supplemented with 1% digitonin (w/v) and nutated for 1 h at 4°C. Supernatant was cleared by spinning at 20,000 ×*g* speed for 15 min and 2.5% of the supernatant was kept as the input. The rest of supernatant were incubated with anti-FLAG M2 agarose affinity gel nutating at 4°C for 2 h. Beads with bound proteins were washed with IP buffer with 0.1% digitonin (w/v) for 4 times before elution with protein loading dye. All following procedures were performed as the pulse assay.

Seahorse assay

15,000 C2C12 cells or 10,000 C2C12 cells were plated on Seahorse XF96 Cell Culture Microplates (Agilent) 1 day or 2 days before the MitoStress test, respectively. XFe96 sensor cartridge (Agilent) was hydrated with distilled water at 37°C with no CO_2 the day prior to the MitoStress test. Drug treatment was performed 1 day before the assay. On the day of assay, cells were washed once and media were replaced with XF basal DMEM supplemented with 1 mM pyruvate, 2 mM glutamine, and 10 mM glucose OR 10mM galactose. Pre-hydrated sensor cartridge was calibrated with Seahorse XF Calibrant (Agilent). Both cell culture plate and sensor cartridge were incubated at 37°C with no CO_2 for at least 45 min before the assay. For MitoStress assay, 2 μM of oligomycin, 1 μM of FCCP, and 1μM of rotenone/antimycin were injected according to Seahorse MitoStress Assay Protocol (Agilent). Citrate synthase activity was performed for cell number normalization.

Citrate synthase activity assay

Citrate synthase activity was performed on Seahorse XF96 Cell Culture Microplate (Agilent) right after seahorse assay or on plates frozen at −80°C with the leftover medium aspirated. 113 μL of CS buffer (200 mM Tris buffer at pH8.0, 0.2% Triton X-100 (v/v), 100 μM DTNB in 100 mM Tris buffer at pH8.0, 1mM Acetyl-CoA) was added to wells. 5 μL of 10 mM oxaloacetic acid was added as the reaction substrate. Absorbance at 412 nM at 37°C was recorded with a Tecan Microplate Reader M200 (Tecan) at a minimal time interval for 5 min.

Citrate Synthase activity was then calculated using the formula below

$$\text{CS activity} = \sum_{i=1}^{n}\left(\left[\frac{A_i - A_0}{t_i - t_0}\right]\right) \Big/ n \; (n \in N^*)$$

n is the total number of absorbance records; A is the absorbance recorded; t is the time.

GFP competitive assay

WT C2C12 cells expressing GFP were seeded together with C2C12 cells line that need to be tested at the ratio of 1:1 in 12 well plates. Percentage of GFP positive cells was quantified every 3 passages on day 8 and day 16. Co-culture of GFP positive cell with cells with growth defects should show increased GFP percentage and vice versa.

Quantitative PCR assay

Total RNA was extracted from respective cell lines using TRIzol. cDNA was obtained using iScript Reverse Transcription Kit. Quantitative measurement of cDNA amount was done using iTaq SYBR Green Kit and CFX384 Touch Real-Time PCR Detection System. All primers used were included in the key resource table.

QUANTIFICATION AND STATISTICAL ANALYSIS

Immunoblots were quantified using the volume tool of Image Lab (Version 6.0.1) with default background subtraction setting. Phosphor images were quantified using Image J. Statistical tests were performed using GraphPad Prism (Version 8). Two-tailed unpaired t test was performed as indicted in the figure legend of specific experiments. p value <0.05 is used as the cut off of significant different in this study. Actual levels of significance were marked in figure panels. No data point was excluded for data analysis.